Mechanism of Low Frequency Spectral Scattering by a Side-Branch Electromagnetic Device with Switching Shunt

Lixi Huang[*,1,2], Keming Wu[1] Xue Han[1] and Yumin Zhang[2,3]

[1]Department of Mechanical Engineering, The University of Hong Kong, Pokfulam, Hong Kong, China

[2]Lab for Aerodynamics and Acoustics, The University of Hong Kong Zhejiang Institute of Research and Innovation, 1623 Dayuan Road, Lin An District, Hangzhou, Zhejiang, China

[3]Foshan University, 33 Guangyun Road, Shishan, Nanhai District, Foshan, Guangdong, China

Abstract: Sound waves are reflected and absorbed by a passive side-branch device in a duct. The performance is limited at low frequencies if the cavity is compact. In this study, an electro-magnetic mechanism to enhance such low-frequency performance is examined. A common loudspeaker diaphragm, with its moving-coil immersed in the magnetic field, is used as a passive interface to the cavity, and a shunt analogue circuit is periodically connected and disconnected by a MOSFET. When the diaphragm is driven to vibrate by the incident wave, the reactive Lorentz force exerts extra acoustic impedance, which almost stops the diaphragm vibration if the shunt is close to a short circuit. The repeated transition between system damping of very low and high values scatters a significant portion of the incident sound energy to frequencies other than the source frequency. The peak energy scattering efficiency is found when the switching is twice the frequency of the incident. The sudden removal of the Lorentz force by MOSFET switch-off creates a boost in the diaphragm response, which is otherwise suppressed by the cavity stiffness, leading to much enhanced sound reflection. When the incident wave is random with a finite frequency band, scattering effect is found to offer a positive virtual mass, which counters the high system stiffness in the low frequencies.

Keywords: spectral scattering, duct noise control, electro-magnetic diaphragm, switching shunt, low-frequency sound

1. Introduction

Broadband noise control remains a great technical challenge to acousticians. To be specific, we define "broadband" to be a frequency range that very much exceeds an octave band, such as a decade. We shall call a bandwidth near one octave band as "finite-band", and the range well below this to be a narrow band, single-frequency being its extreme. As we can soon appreciate from basic dynamics of all basic materials and structures, bandwidth very much dictates what is possible, and a discussion without reference to bandwidth can be misleading. For instance, one cannot compare the performance in a narrow stopband (or bandgap) of a resonating device with the seemingly low performance of a broadband device that operates at frequencies far away from its own resonance.

In a flow duct, silencers must be installed in a side branch. The dynamics of such configuration differs significantly from the normal incidence. This configuration is traditionally called grazing incidence and

[*]Corresponding author. Telephone: (852) 39172627. Email addresses: lixi.huang@hku.hk (L. Huang), kemingwoo@foxmail.com (K. Wu), hanxue929@connect.hku.hk (X. Han), yumin@connect.hku.hk (Y. Zhang)

some recent literature calls it "ventilated" mode. It is well known that the use of porous material along a duct, namely duct lining, is technically satisfactory in the medium to high frequency regions. To be more specific, we define "medium" frequency to be the range whose half-wavelength is comparable with the duct height. Micro-perforated panels (MPP) can also serve as the dissipative element in a silencer, but there is no fundamental difference in acoustics between an MPP and fibrous materials. MPP has the practical advantage of being hygienic but it comes at a high manufacturing cost when very high levels of dissipation is desired. What is missing technologically is the low-frequency performance for duct noise control. A large volume is needed to tackle this over a reasonably broad frequency band in the low frequency region, such as the octaves centred at 63, 125 and 250 Hz. Existing good designs use a hybrid of sound absorption and reflection [1-2], but a higher-level of hybrid using active and passive controls [3] is theoretically more promising. In reality, the latter is not widely used as engineers favour pure passive control with good robustness and low cost. Advances in acoustic metamaterials (AMM) have raised the prospect of a smart passive device [4-6] performing better than the classical hybrid designs. Before discussing AMM in a broader sense, we would like to bring up the concept of optimal impedance.

What is mathematically possible for duct noise control was examined by Cremer [7], and the result of that study is appropriately called the Cremer impedance in later literature. Though not strictly proven, the best locally reactive impedance is achieved when eigen-values of two lowest order modes in a lined duct converge, leading to the so-called exceptional point or branch point in the complex plane [8-11]. This impedance condition certainly points to the direction of superior performance in duct noise control, but caution is also needed for the following reasons. First, the model is based on a duct liner of infinite length. It is reasonable to suspect that a short device has different answers for the optimal interface impedance. Second, the optimal impedance is a function of frequency, which means that a true metamaterial must follow an ideal mathematical curve of material properties. Such a design is yet to be materialized. Third, the total noise reduction is determined by the incident wave spectrum. There is no such thing as an optimal impedance for all noise problems. Having said that, pink noise incidence would be a good benchmark to start with as most industrial and environmental noise problems have energy concentrated towards low frequencies. As pointed out by Tester [8], the benefit of the Cremer impedance is only valid when the prevailing incident noise is indeed dwelling in the least-decaying modes. Besides, the onus to achieve the identified Cremer impedance is by no means trivial at low frequencies. For instance, Tester [8] gave the following optimal impedance for a rectangular duct without flow as $p/(\rho_0 c_0 v) = (0.929 - 0.744\,\mathrm{i})kh_0/\pi$, where $\rho_0 c_0$ is the specific air impedance and kh_0 is the Helmholtz number of the duct of height h_0. If the duct liner has a cavity depth of h_{cav}, the negative dimensionless reactance provided by the cavity alone is $\cot(kh_{\mathrm{cav}})$. Therefore $0.744kh_0/\pi = \cot(kh_{\mathrm{cav}})$. For the typical example we shall treat in this study, $h_0 = 0.1\mathrm{m}$, $f = 150$ Hz, it means a rather deep cavity of $h_{\mathrm{cav}} \approx 0.55$ m. Interestingly, the optimal resistance is found to be negative when frequency approaches zero [9]. We can therefore conclude that we are dealing with a very different question here. What we are interested to know is what is possible for a shallow cavity such as $h_{\mathrm{cav}} = h_0 = 0.1$ m as a given condition. For such a geometry, the Cremer impedance is partially satisfied when $f \approx 700$ Hz, which is clearly in the medium frequency range. In the language of the AMM community, the problem of $f = 150$ Hz using $h_{\mathrm{cav}} = h_0$ is in the deep subwavelength range. In a related development of active impedance control [12], desirable impedance with prescribed system mass, resistance and compliance is achieved through sending the right electrical current through the shunt circuit of a side-branch diaphragm based on the average acoustic pressure sensed on the diaphragm.

In the past decade or so, various smart structural designs, known as acoustic metamaterials (AMM), have enjoyed successes following the footsteps of optical metamaterials for cloaking and super-resolution imaging [13-14]. To achieve low-frequency wave manipulation is one of many worthy goals of AMM nowadays. However, a comprehensive comparison with classical passive noise control techniques or hybrid active-passive control is yet to be performed to take stock of the current status of

AMM. One of the most interesting topics in AMM is the so-called acoustic non-reciprocity [15], which seems to have direct bearing on duct noise control. It would be intuitively appealing if sound from left were allowed to travel to the right but not the other way round. It remains to be seen, however, how much "resources" we need to deploy to achieve such non-reciprocity and to what extent it bears fruit in broadband noise control. By "resources" we mean the volume occupied by the controller device, instead of the manufacturing cost, in the context of low-frequency broadband noise. In an informal AMM review, Haberman and Norris [16] point out that traditional Helmholtz resonator has always been compact, and the line between AMM and classical acoustics is not distinctive. Like any other mechanical resonator, a Helmholtz resonator achieves resonance when the inertia effect balances the stiffness. Low frequencies are stiffness controlled but it is always possible to add inertia, such as by adding a thin membrane, whose material density is thousands of times higher than air, to bring down the resonance frequency down to zero. The consequence of doing so is that the bandwidth will also vanish. It is therefore compulsory to present some measure of total wave energy reduction when discussing the merits of any resonator-based designs. Classical designs using parallel arrangement of MPP resonators [17, 4] or Helmholtz resonators in series [18-19], or meticulously detuned resonators in series [20] have already demonstrated high levels of sound absorption within a finite frequency band. In such studies, the trade-off between bandwidth and the total device performance is apparent. The device volume as the control parameter can be explicitly formulated using a causality-based integral approach [21-22]. In terms of the interface impedance for the grazing incidence, the resonator volume, or the system compliance, is represented by the negative reactance analyzed in this study. The question we ask is the following: is it possible to achieve a reduction in the magnitude of the interface reactance for a given cavity depth without invoking the usual resonance mechanism that will inevitably limit the bandwidth?

As a typical noise spectrum is "pink", in which the intensity is nearly inversely proportional to the frequency, the overall performance of a duct liner crucially depends on how much noise is reduced for the lowest frequency components. It is very "expensive" to allocate enough space for a low-frequency resonator with a useful bandwidth. An optimization program can be set up for the sound absorption performance for a given total side-branch volume. Instead of going down this path of design optimization, this study aims to explore a different strategy of noise control: linear frequency conversion, which is also described as spectral scattering in the subsequent text. Specifically, we introduce a time-varying liner property that modulates the incident sound such that some energy in the low-frequency region is converted to higher frequencies that can be handled more easily by other mature techniques. For example, in our main example for an incident sound of 150 Hz, a modulation at 300 Hz converts part of the sound energy to 450 Hz, which is fairly easy to absorb.

Frequency shift is also commonly found in nonlinear materials, which are sometimes called dynamic materials and can be regarded as the first generation of time-varying materials [23-24] with a possible link to the concept of time crystals [25]. Its time-varying properties, such as stiffness, is dynamically dependent on the excitation amplitude. The amplitude at which nonlinear effect is significant can be impractically high. An attempt to introduce active nonlinearity at low excitation amplitude [26] succeeded in broadening the sound absorption around the nonlinear resonance, but the high coefficient for the nonlinear-term needed in the control law may cause saturation and the beneficial nonlinear effect remains amplitude-dependent. A linear mechanism of frequency conversion is much more desirable, and the crucial parameter for success is the modulation ratio. The best performance is likely to be derived from designs that do not depend on narrow-band resonances. In what follows, we modify the shunt circuit used in [27-28] to exclude the capacitor so as to avoid electrical resonance, and refrain from adjusting any structural design such that the mechanical system will remain at some distance from resonance in frequency. Section 2 introduces the plane-wave theory suitable for low-frequency studies in the electro-mechanically coupled system. This is done with both analytical formulation in frequency-domain and time-domain numerical simulation. The latter is validated by the exact frequency-domain results. Section 3 describes the typical example with details of energy conservation analysis. Finally,

the results of time-domain simulation is Fourier transformed to seek frequency-domain understanding of the main spectral scattering mechanism. It is shown that MOSFET switching neutralizes a significant part of the cavity reactance leading to improved noise reduction performance. Conclusions are drawn in Section 4.

2. Basic theory and numerical method

2.1 Side-branch device without shunt switching

In this particular realization, we use an electro-magnetic diaphragm shunted by an analogue circuit, illustrated in Figure 1(a). The diaphragm can be specially made or can be a commercially available loudspeaker for convenience. Instead of generating sound as is normally intended for, an incident sound pushes a passive diaphragm whose moving coil cuts through the magnetic field. When a shunt circuit connects the coil in a loop, the generated electrical charges flow. The induced current through the moving coil induces the Lorentz force, which is a reaction force against the incursion by the diaphragm, in a way like a mechanical spring. The shunt circuit only consists of passive elements like a resistor, capacitor and inductor. Since the coil has inductance, we may not need any extra inductance. In any

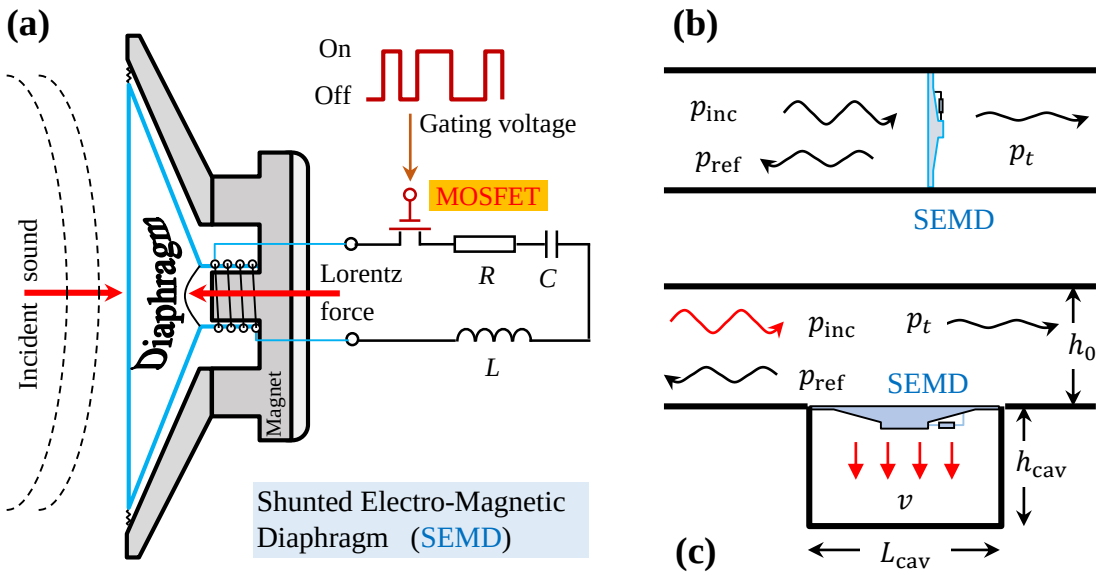

Figure 1. The basic module and two configurations of study. (a) The construction of shunted electro-magnetic diaphragm (SEMD). The square wave train on the upper-right represents the voltage supplied to the "Gate" terminal of MOSFET which connects or disconnects the RCL shunt circuit. (b) SEMD used to stop the incident sound wave (p_{inc}) from transmitting through in a duct. (c) SEMD used as a sound absorber or scatterer in a side-branch to minimize sound transmission (p_t) downstream. The cavity size is h_{cav} by L_{cav}, while the duct height is h_0. Incident sound pushes the diaphragm into the cavity at a surface-averaged velocity v, which radiates sound to both sides.

case, we shall use L to represent the total inductance in the shunt. The diaphragm used in this special manner is denoted as Shunted Electro-magnetic Diaphragm, or SEMD, in all subsequent discussions. The simplest method of achieving the time-variation of the acoustic property, or modulation, is to use a MOSFET (metal–oxide–semiconductor field-effect transistor) to dynamically connect or disconnect the shunt circuit, as demonstrated in our recent study [28]. A voltage is supplied to the "Gate" terminal of the transistor. When this voltage exceeds a threshold, such as 5 v, the MOSFET connects the shunt circuit, which is described as "shunt-on" state; otherwise, the transistor presents a high resistance of several thousands of Ohms, and the shunt circuit is effectively disconnected. The switching takes place over nano-seconds and it is considered as instant. The connection and disconnection is specified by the square wave train illustrated in the upper right side of Fig. 1(a). The frequency of switching is thus the

modulation frequency. Despite the appearance of being "active" in achieving such modulation, the switching action is pre-programmed and it should not act in response to any detection signal in an active control scheme. There is no energy exchange between the circuit and the mechanical vibration during the switching event, and the system is effectively passive. Switching shunt has also been used in vibration control, but it remains to be seen if it is effective for our acoustic purpose.

Figure 1(b) was the configuration used in our recent study [28]. It was experimentally demonstrated that part of the sound energy in the source (incident) frequency f_s was scattered into numerous sidebands of frequency $f_s \pm nf_m$, where f_m is the modulation (switching) frequency by the MOSFET, and $n = 1$ is the dominant order of modulation. It was also demonstrated that, when a pure tone of frequency f_s was modulated by a random switching pattern with a frequency range of $f_m \in (f_1, f_2)$, the generated output in the first-order sideband also had the linear bandwidth of $f_2 - f_1$. In other words, a pure tone was scattered into a banded signal. By suitably choosing the switching frequency range, f_m, part of the incident sound energy was converted to infrasound, $f_s - f_m < 20$ Hz. The purpose of the current study is to explore how effective the system can be for the grazing incidence configuration shown in Fig. 1(c), which is more applicable in duct noise control. For this purpose, a cavity must be provided to prevent sound leakage, and its size, $h_{\mathrm{cav}} \times L_{\mathrm{cav}}$, very much determines the silencing performance for traditional duct liners in the low-frequency regime. This is so because the air stiffness in a compact cavity suppresses the acoustic response in the side-branch, allowing the sound to transmit directly to downstream. It will be shown below that the switching shunt can effectively neutralize the cavity stiffness effect when a suitable modulation frequency is chosen.

In order to focus on the basic mechanisms of spectral scattering, the frequency is assumed to be in the cut-off region, $f \ll c_0/(2h_0)$. As shown in Fig. 1(c), the diaphragm responds to the incident wave and its retreat into the cavity at velocity $v(t)$ creates a negative pressure wave into the upstream, forming the reflection pressure, p_{ref}, and cancels part of the incident wave pressure in the downstream,

$$p_{\mathrm{ref}} = -\rho_0 c_0 v Z_{\mathrm{rad}} e^{\mathrm{i}(\omega t + k_0 x)}, \qquad p_t = p_{\mathrm{inc}} - \rho_0 c_0 v Z_{\mathrm{rad}} e^{\mathrm{i}(\omega t - k_0 x)}, \tag{1}$$

$$Z_{\mathrm{rad}} = \mathrm{Re}\left(\frac{p_{\mathrm{rad}}}{\rho_0 c_0 v}\right) = \left(\frac{L_{\mathrm{cav}}}{2h_0}\right), \tag{2}$$

where $k_0 = \omega/c_0$ is the wavenumber, and Z_{rad} is the real part of the radiation impedance normalized by the specific air impedance $\rho_0 c_0$. At low frequencies, the volume flux by the vertical motion of the diaphragm is simply converted to the horizontal fluxes in the upstream and downstream, each with half share at the absence of a mean flow. The radiation loading on the diaphragm has a part in phase with the velocity, $\rho_0 c_0 v Z_{\mathrm{rad}}$, as well as a part out-of-phase with the velocity. The latter has been analyzed in details by Huang [29] with the pressure expanded into rigid duct modes. It is concluded that the sum of the out-of-phase parts approximately amounts to the effects of a negative virtual mass and has an interesting physics. If the upper duct wall is mathematically replaced by a mirror, its constraining effects on the sound field is represented by a series of image sources, the one right above the upper wall being dominant. This image source radiates in the same time phase as the actual one and its radiation pressure, which is in phase with the vibration velocity, is time delayed by $2h_0/c_0$ as it is located at a distance $2h_0$ above the lower wall. The delayed radiation resistance force is partially converted to the negative mass. The amount of negative mass thus incurred is equivalent to an air column of length L_{cav} and is considered to have a minimal impact on the diaphragm dynamics, especially in the low-frequency region. Alternatively, one may lump this into the diaphragm mass. Thus simplified, the pressure continuity and volume flux conservation for the junction enclosing the diaphragm region for Fig. 1(c) read, assuming the origin of $x = 0$ at the centre of the device,

$$p_{\mathrm{inc}} + p_{\mathrm{ref}} = p_t, \qquad (p_{\mathrm{inc}} - p_{\mathrm{ref}})h_0 = p_t\left(h_0 + Z_{\mathrm{int}}^{-1} L_{\mathrm{cav}}\right), \tag{3}$$

where Z_{int} is the dimensionless interface impedance of the cavity-backed diaphragm, which consists of contributions from structural elements (mass, mechanical damping, diaphragm suspension stiffness and cavity stiffness) and from the Lorentz force when the shunt circuit is connected by MOSFET,

$$Z_{\text{int}} = \frac{p}{\rho_0 c_0 v}\bigg|_{\text{interface}} = \left[mi\omega + d_m + \kappa'(\mathrm{i}\omega)^{-1} + \frac{(Bl)^2}{Z_e}\right]/d_0, \tag{4a}$$

where

$$\kappa' = \kappa + \frac{\rho_0 c_0^2 h_0^2}{h_{\text{cav}}}, \quad d_0 = \rho_0 c_0 h_0^2. \tag{4b}$$

Here, we have taken the liberty to use m, d_m, κ to denote the mass, damping and stiffness per unit diaphragm area equal to h_0^2. Constant d_0 is the resistance of sound radiation in a duct of cross section h_0^2. This scheme of notation will bring the following benefits. When a larger diaphragm is needed, such as two square-shaped loudspeakers to implement a cavity length of $L_{\text{cav}} = 2h_0$, the parameters m, d_m, κ remain unchanged. The parameter (Bl) is the force factor, B being the magnetic flux density and l the effective coil length. Under the scheme of measuring everything per unit area h_0^2, one assumes L_{cav}/h_0 sets of such square-shaped diaphragm, each with the same Bl and the same set of electrical circuit whose electrical impedance is

$$Z_e = L\mathrm{i}\omega + R + \frac{1}{C\mathrm{i}\omega}. \tag{5}$$

Here, L and R already include the coil inductance and resistance, respectively. Solving Eq. (3), we obtain the complex, linear transmission coefficient and reflection coefficient,

$$\frac{p_t}{p_{\text{inc}}} = \frac{Z_{\text{int}}}{Z_{\text{int}} + Z_{\text{rad}}}, \qquad \frac{p_{\text{ref}}}{p_{\text{inc}}} = \frac{-Z_{\text{rad}}}{Z_{\text{int}} + Z_{\text{rad}}}. \tag{6}$$

Note that Z_{rad}, given in Eq. (2), is derived from the mass flux term with L_{cav} in Eq. (3). It is important to note that, by such modular construction of devices, Z_{int} is independent of the length L_{cav}, which is solely reflected in Z_{rad}. In an experimental implementation for $L_{\text{cav}} = 2h_0$, one can use two square loudspeakers to occupy the whole lateral width of a square duct and the axial length is L_{cav}. Alternatively, one can take one of the two square loudspeakers to be placed on the sidewall and the volume flux into or out of the duct will have the same effect as two loudspeakers in tandem.

Detailed physics of each shunt circuit component are explained by Zhang et al. [30]. When the shunt circuit has no capacitor ($C = \infty$), and no inductor ($L = 0$), which is impractical in this design due to the use of the coil, the electro-magnetically induced acoustic impedance, $(Bl)^2/R$, would amount to a pure mechanical damping inversely proportional to R. The presence of the inductor L complicates the phase relation. Wu et al. [31] experimentally demonstrated that a negative impedance converter could be used to minimize the inductance effect as well as the residual resistance embedded in the coil, and in the connecting wires, to approximate a true short circuit, $R \to 0$. A very high sound isolation effect for Fig. 1(b) was achieved with extremely broad frequency band well over a decade. When $R = 0, C = \infty$, an inductor-only shunt circuit would mean an electro-magnetic spring of stiffness $(Bl)^2/L$. This effect is surely present in the analysis of the next section although we will certainly allow a small resistor R as any practical inductor should have. In the current theoretical study, we retain part of the natural inductance existing in the chosen loudspeaker, but will explore the effect of reduced circuit resistance $R \to 0$, which is physically viable if the device is tailor-made instead of being constrained by commercially available products.

In order to investigate details of spectral scattering mechanism, we first limit ourselves to the example of one single incident wave frequency, f_s, but we avoid any effect of resonance in the hope that the

result is applicable to a wide frequency band. Specifically, the capacitor is removed, $C = \infty$, so that there is no circuit resonance at a finite frequency. The structural mass is taken from the natural loudspeaker diaphragm, and the structural resonance frequency is higher than that in the incident sound wave.

The structural damping coefficient in a realistic loudspeaker varies with frequency. For the sake of simplicity of this theoretical investigation, we keep it as a constant and allow the damping to be specified according to theoretical needs. The coefficients of sound energy reflection (β), transmission (γ), and absorption (α), are defined below,

$$\beta = \left|\frac{p_{\mathrm{ref}}}{p_{\mathrm{inc}}}\right|^2, \qquad \gamma = \left|\frac{p_t}{p_{\mathrm{inc}}}\right|^2, \qquad \alpha = 1 - \beta - \gamma, \tag{7}$$

which can be analytically calculated from Eqs. (2), (4), (5) and (6) when the device is without MOSFET. With MOSFET switching, analytical calculation would become impractical as the device response at any one frequency is coupled with the property at all others [28]. In such case, numerical simulation has to be employed and the results of $p_t/p_{\mathrm{inc}}, p_{\mathrm{ref}}/p_{\mathrm{inc}}$ are analyzed by Fourier transforms to yield the spectra of sound absorption, reflection and transmission. Energy conservation check to be conducted later refers to the comparison of α calculated from the acoustic part here with the sum of components of energy damping calculated from structural damping and Joule heating in the circuit.

Figure 2 shows the sound energy transmission coefficient γ before shunt switching technique is applied. Figure 2(a) is for the single source frequency of $f_s = 150$ Hz but the design parameters vary. Figure 2(b) is the performance of the device for all frequencies when the design parameter is optimized for $f_s = 150$ Hz. The best design parameters are identified as the trough points in Fig. 2(a). The essential purpose of this figure is to show what the best is for SEMD without MOSFET, and this will serve as a basis to study the effects of shunt switching.

In Fig. 2(a), the solid curve is for the shunt-off design and the abscissa is $\bar{d} = d_m/d_0$. The filled circle gives the best performance of $\gamma_{\min} = 0.75$ when $d_m/d_0 = 3.01$. The loudspeaker used in [28] has $d_m/d_0 = 1.20$, meaning that it is very much below the optimal for this frequency. The dashed line is for the design with shunted circuit but with structural damping $d_m = 0$, and the abscissa is the electrically induced damping normalized by d_0, namely $\bar{d} = (Bl)^2/(Rd_0)$. The best performance (open-squares) is $\gamma_{\min} = 0.77$, slightly worse than the shunt-off as the inductance increases the system stiffness.

The reason for the troughs in Fig. 2(a) can be easily analyzed by the transmission coefficient γ in Eq. (6). Suppose the interface impedance is split into real and imaginary parts as $Z_{\mathrm{int}} = Z_r + \mathrm{i}Z_i$, minimal transmission is achieved when $\partial\gamma/\partial Z_r = 0$ for a given condition of Z_i mainly determined by the cavity stiffness, diaphragm stiffness and the shunt inductance. Combining the definition of γ in Eq. (7) and the complex transmission ratio in Eq. (6), we obtain

$$\gamma = \frac{Z_r^2 + Z_i^2}{(Z_r + Z_{\mathrm{rad}})^2 + Z_i^2}, \qquad \left.\frac{\partial\gamma}{\partial Z_r}\right|_{Z_r = Z_{r,\mathrm{opt}}} = 0 \rightarrow Z_{r,\mathrm{opt}} = \sqrt{Z_i^2 + (Z_{\mathrm{rad}}/2)^2} - (Z_{\mathrm{rad}}/2). \tag{8}$$

At side-branch resonance, $Z_i = 0$, the optimal real part will be with zero damping when all sound is reflected. However, when the system is far from resonance, as is the case for a compact-cavity-backed device, $Z_i \rightarrow -\infty$, the optimal design would be $Z_{r,\mathrm{opt}} \approx |Z_i|$. In other words, a high damping is needed to match the high system stiffness. At the optimal damping setting, the optimal transmission is

$$\gamma_{\min} = \frac{\sqrt{Z_i^2 + (Z_{\rm rad}/2)^2} - (Z_{\rm rad}/2)}{\sqrt{Z_i^2 + (Z_{\rm rad}/2)^2} + (Z_{\rm rad}/2)} \xrightarrow{Z_i \to -\infty} 1 - \frac{Z_{\rm rad}}{|Z_i|}. \tag{9}$$

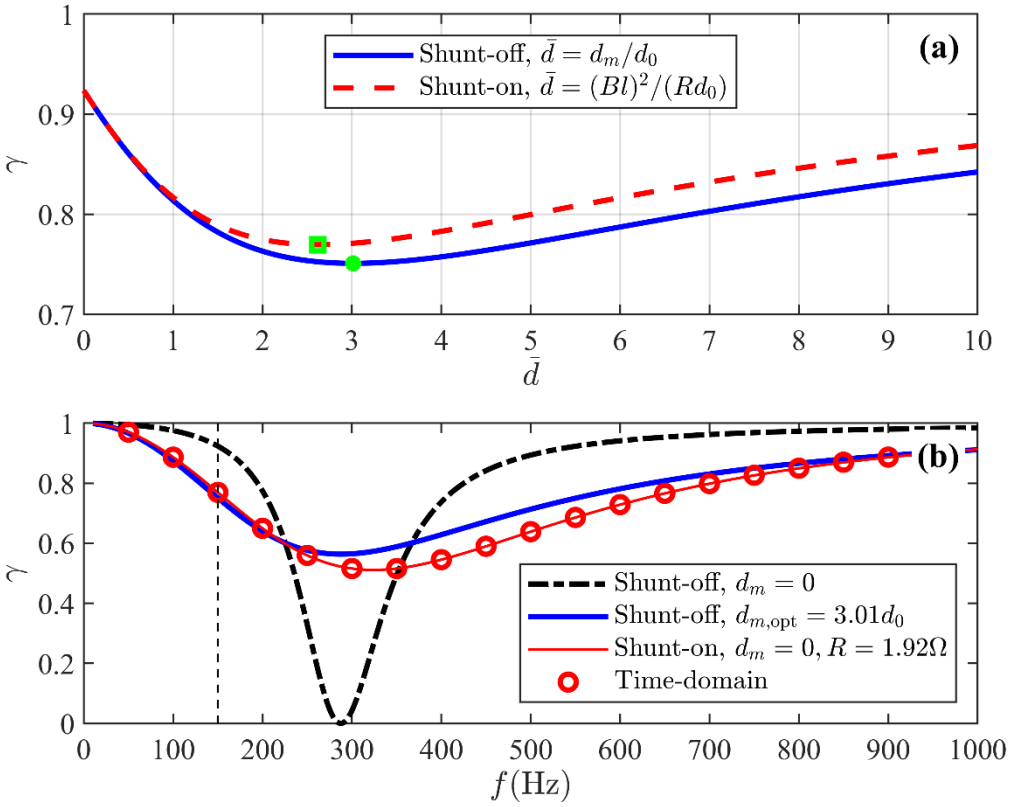

Figure 2. Optimal performance for the shunt-off design and the validation of time-domain computation by the frequency-domain solution. (a) Transmission coefficient γ for the incident sound with $f_s = 150$ Hz when different energy dissipations are used, showing the best designs highlighted by an open square and a filled circle. The solid line is the design without shunt circuit and the abscissa is $\bar{d} = d_m/d_0$. The dashed line is for SEMD with electrical damping but without structural damping, $d_m = 0$, and the abscissa is the electrically induced, normalized, mechanical damping parameter $\bar{d} = (Bl)^2/(Rd_0)$. (b) Transmission spectrum for a fixed set of design parameters. The thick solid line is with the optimal structural damping identified in (a) as the filled circle. The thin solid line is for SEMD with the best electrical resistor identified in (a) as the open-square. The open-circles along this line is the result of time-domain calculation at these chosen frequencies. The dash-dot line is the shunt-off design without structural damping. Other parameters used are $m = 5.8$g, $\kappa = 4516\text{N m}^{-1}, h_0 = h_{\rm cav} = 0.1\text{m}, L_{\rm cav} = 2h_0, L = 0.2$ mH, $\text{C} = \infty, Bl = 4.6$ Tm.

It is easily checked that the trough for the shunt-off design in Fig. 2(a) conforms to the result of Eqs. (8) and (9). The same is true with the shunted design but the calculation for Z_i is more complicated. The last part of Eq. (9) implies that sound transmission can be reduced by increasing $Z_{\rm rad}$ via cavity length $L_{\rm cav}$, cf. Eq. (2), which will be presented later in Fig. 6.

Figure 2(b) gives the transmission spectrum when the device is optimized for $f_s = 150$ Hz only, which is marked by a vertical dashed line. The dash-dot line is an un-shunted diaphragm without damping, giving a resonance at 287.5 Hz where all sound is reflected and $\gamma = 0$. The vertical dashed line highlights the fact that the frequency of $f_s = 150$ Hz is well within the stiffness-controlled region for which the optimal passive design (thick solid curve) can only provide $\gamma_{\min} = 0.75$, which means a

transmission loss of TL $= -10\lg 0.75 = 1.25$ dB. The thin solid curve is for the shunted design with all structural damping removed in favour of electrical damping of $R = 1.92\Omega$ optimized for $f_s = 150$ Hz. Its performance for higher frequencies is generally better than the pure mechanical design by a small margin. The open-circles are the results from the time-domain numerical simulation, for which the deviation from the analytical frequency-domain solution is not discernable. Having said that, this validation is without MOSFET switching. With MOSFET switching, there can be no analytical result. However, the same simulation method for the configuration shown in Fig. 1(b) has been compared with experiment in [28] with very close agreement. It is pointed out that a perfect agreement with experiment is not expected, as there are quite a number of measurement uncertainties. We are therefore satisfied with the time-domain solution, which is briefly outlined below for the current configuration in Fig. 1(c), but without the special normalization scheme used in [28] for simplicity.

2.2 Time-domain solution method

The governing equation for the motion of the diaphragm under the incident wave pressure $p_{\text{inc}}(t)$ is

$$m\frac{\mathrm{d}v}{\mathrm{d}t} + d'v + \kappa'\eta + BlI = h_0^2 p_{\text{inc}}(t), \;\; d' = d_m + Z_{\text{rad}}d_0 \tag{10}$$

where $v = \mathrm{d}\eta/\mathrm{d}t$ is the vibration velocity, η is the displacement, κ' is the device stiffness inclusive of the cavity contribution, cf. Eq. (4b), I is the electric current in the shunt circuit. The term $Z_{\text{rad}}d_0$ in d' accounts for the radiation pressure $-\rho_0 c_0 v Z_{\text{rad}}$ acting on the diaphragm of one unit area h_0^2. The governing equation for the shunt circuit is given below together with more parameter definitions,

$$L\frac{\mathrm{d}I}{\mathrm{d}t} + R(t)I + \frac{q}{C} = Blv, \qquad I = \frac{\mathrm{d}q}{\mathrm{d}t}, \tag{11a}$$

$$R(t) = R_{\text{on}} + R_{\text{off}}[1 - g(t)], \;\; g(t) = 1(\text{MOSFET on}); 0(\text{MOSFET off}). \tag{11b}$$

Here, q is the electrical charge, $R(t)$ is the instantaneous electric resistance, R_{on} is the total circuit resistance when MOSFET is switched on, and R_{off} is the huge resistance value when MOSFET is switched off. The coupled second order Equations (10) and (11) are cast as a set of four first-order equations in matrix form,

$$\frac{\mathrm{d}}{\mathrm{d}t}\underbrace{\begin{bmatrix} v \\ I \\ \eta \\ q \end{bmatrix}}_{\mathbf{U}} + \underbrace{\begin{bmatrix} d'/m & Bl/m & \kappa' & 0 \\ -Bl/L & R(t)/L & 0 & 1/(LC) \\ -1 & 0 & 0 & 0 \\ 0 & -1 & 0 & 0 \end{bmatrix}}_{\mathbf{D_M}} \underbrace{\begin{bmatrix} v \\ I \\ \eta \\ q \end{bmatrix}}_{\mathbf{U}} = \underbrace{\begin{bmatrix} p_{\text{inc}}h_0^2/m \\ 0 \\ 0 \\ 0 \end{bmatrix}}_{\mathbf{F}}, \tag{12}$$

where $\mathbf{D_M}$ is the damping matrix. Equations (12) degenerate into a set of three equations when the capacitor is absent, $C = \infty$, as there is no need to calculate the electrical charge q from the current I, or two equations for v and η when the MOSFET is switched off with $I = 0$. The time-domain solution is easiest when it is separated into two states of MOSFET-on, $R(t) = R_{\text{on}}, g(t) = 1$, and MOSFET-off, $R_{\text{off}} \to \infty, g(t) = 0$. All material properties are constant during the shunt-on and shunt-off periods, respectively.

The electric current vanishes at the precise moment of switching, while all other variables in **U** remain unchanged. The electrical charge is held constant during the entire MOSFET-off period,

$$\left.\frac{\mathrm{d}q}{\mathrm{d}t}\right|_{g=0} = 0, \;\; q|_{g=0} = \text{constant}, \tag{13}$$

and the end values of $\mathrm{d}q/\mathrm{d}t$ and q are given as initial values for the four-element state vector **U** in the next MOSFET-on period.

For both states, time-marching from time step t_n to t_{n+1} is given by the usual solution to the first-order differential equations (12), or $\mathrm{d}\mathbf{U}/\mathrm{d}t + \mathbf{D_M}\mathbf{U} = \mathbf{F}$,

$$\mathbf{U}(t_{n+1}) = e^{-\int_{t_n}^{t_{n+1}} \mathbf{D_M}\mathrm{d}t}\left[\mathbf{U}(t_n) + \int_{t_n}^{t_{n+1}} e^{\int_{t_n}^{t} \mathbf{D_M}\mathrm{d}\tau}\mathbf{F}(t)\mathrm{d}t\right]. \tag{14}$$

The matrix exponential may be evaluated by eigen-value decomposition for such small matrix size,

$$-\mathbf{D}_\mathrm{M} = \mathbf{H}\boldsymbol{\Lambda}\mathbf{H}^{-1}, \qquad e^{\int_{t_n}^{t} \mp\mathbf{D_M}\mathrm{d}\tau} = \mathbf{H}\left[e^{\pm\boldsymbol{\Lambda}(t-t_n)}\right]\mathbf{H}^{-1}, \tag{15}$$

but Padé approximation will be more appropriate when a large matrix is involved in two or three dimensional wave propagation computations [32]. Here, $\boldsymbol{\Lambda}$ is the diagonal matrix containing four eigenvalues of the damping matrix, and $\left[e^{\pm\boldsymbol{\Lambda}(t-t_n)}\right]$ is the diagonal matrix whose j'th entry is calculated by the j'th eigenvalue Λ_j as $\exp\left[\pm\Lambda_j(t-t_n)\right]$. For a real-valued problem, we expect eigen-values to emerge as conjugate pairs representing eigen oscillations for the diaphragm coupled to the shunt circuit. Columns in matrix **H** are the corresponding eigen-functions.

Time-marching solution may begin with zero values for all fluctuation variables, when an incident wave is introduced at the next time step. When the solutions are segmented into MOSFET-on and MOSFET-off periods, the eigen-values are constant in each time segment. The exponential functions in Eqs. (14) and (15) effectively represent analytical solutions. The accuracy of the time-marching procedure is mainly dependent on how the integration with the forcing term **F** in Eq. (14) is handled. We employ a four-segment Chebyshev series expansion for each time step, $\Delta t = 1/F_s$, where F_s is the sampling frequency. The accuracy for time marching is at least fourth order. Energy conservation check is conducted below to examine the actual numerical accuracy.

2.3 Energy conservation equations and the validation on numerical accuracy

Multiplying Eq. (10) by velocity v and integrate over time and recognizing that the results for $\int v\mathrm{d}v$ and $\int v\eta\mathrm{d}t = \int \eta\mathrm{d}\eta$ both vanish for stationary processes, we obtain

$$\int (d_m v^2 + BlIv)\mathrm{d}t = \int (h_0^2 p_\mathrm{inc} - d_0 Z_\mathrm{rad} v)v\ \mathrm{d}t\,, \tag{16}$$

for which the term $-d_0 Z_\mathrm{rad} v$ in the right-hand side is rewritten as $-h_0^2\rho_0 c_0 v Z_\mathrm{rad}$ and hence $h_0^2 p_\mathrm{ref}$ via Eq. (3a). The whole right-hand side becomes RHS $= \int h_0^2(p_\mathrm{inc} + p_\mathrm{ref})v\mathrm{d}t$. The latter can be further transformed into a form of net acoustic energy input to the diaphragm via the relationship of $p_t = p_\mathrm{inc} + p_\mathrm{ref}$, c.f. Eq. (3a), as follows, $p_\mathrm{inc}^2 - p_\mathrm{ref}^2 - p_t^2 = p_\mathrm{inc}^2 - p_\mathrm{ref}^2 - (p_\mathrm{inc} + p_\mathrm{ref})^2 = -2p_\mathrm{ref}(p_\mathrm{inc} + p_\mathrm{ref})$. Since $p_\mathrm{ref} = -\rho_0 c_0 v Z_\mathrm{rad}$, cf. Eq. (1a), and that $Z_\mathrm{rad} = L_\mathrm{cav}/(2h_0)$, we obtain

$$p_\mathrm{inc}^2 - p_\mathrm{ref}^2 - p_t^2 = \rho_0 c_0 v(L_\mathrm{cav}/h_0)(p_\mathrm{inc} + p_\mathrm{ref}). \tag{17}$$

The right-hand side of Eq. (16) evolves as follows

$$\int (h_0^2 p_\mathrm{inc} - d_0 Z_\mathrm{rad} v)v\ \mathrm{d}t = \int h_0^2(p_\mathrm{inc} + p_\mathrm{ref})v\mathrm{d}t = \frac{h_0^2}{L_\mathrm{cav}}\int h_0 \frac{p_\mathrm{inc}^2 - p_\mathrm{ref}^2 - p_t^2}{\rho_0 c_0}\mathrm{d}t\,. \tag{18}$$

When Eq. (16) is multiplied by L_cav/h_0^2, it transforms the energy integration per unit diaphragm area of h_0^2 into the diaphragm area per unit width perpendicular to the plane shown in Fig. 1(c). The integration in the right-hand side of Eq. (18), such as $\int h_0 p_\mathrm{inc}^2/(\rho_0 c_0)\mathrm{d}t$, then becomes the sound energy for the duct cross section with one unit of width. Finally, all energy integration is normalized by the incident wave energy, E_inc defined below, to obtain the energy conservation in the form of energy coefficients,

$$E_{\text{inc}} = \int h_0 \frac{p_{\text{inc}}^2}{\rho_0 c_0} \mathrm{d}t\,, \qquad \alpha_{dm} = \frac{L_{\text{cav}}}{E_{\text{inc}} h_0^2} \int d_m v^2 \mathrm{d}t, \;\; \alpha_x = \frac{L_{\text{cav}}}{E_{\text{inc}} h_0^2} \int BlIv \mathrm{d}t\,, \tag{19}$$

$$\alpha_{dm} + \alpha_x + \beta + \gamma = 1. \tag{20}$$

Here, α_{dm} is the mechanical damping coefficient, α_x is the coupling energy flowing into the electrical circuit, β and γ are, respectively, the acoustic sound reflection and transmission coefficients defined in Eqs. (7). The total sound absorption coefficient as defined in Eq. 7(c) is thus $\alpha = \alpha_{dm} + \alpha_x$.

The coupling energy flow into the circuit is examined by multiplying Eq. (11a) with the current I and integrating over time,

$$\int \left(L \frac{\mathrm{d}I}{\mathrm{d}t} + R(t) I + q C^{-1} \right) I \, \mathrm{d}t = \int BlIv \, \mathrm{d}t\,. \tag{21}$$

The main complication here is the switching-off moments at times $t_{\text{off}}(n)$ where n is the counting index. Around $t_{\text{off}}(n)$, both current and resistance experience rapid changes. A proper treatment for the integration is made by considering a small time interval Δt before and after the switching action, which will be allowed to vanish. Over this short time, both vibration velocity v and electrical charge q are continuous. When $\Delta t \to 0$, the integrations involving the capacitor and the Lorentz force both vanish, yielding

$$\lim_{\Delta t \to 0} \int_{t_{\text{off}}(n)-\Delta t}^{t_{\text{off}}(n)+\Delta t} \left(L \frac{\mathrm{d}I}{\mathrm{d}t} + R(t) I \right) I \, \mathrm{d}t = 0, \tag{22a}$$

$$\lim_{\Delta t \to 0} \int_{t_{\text{off}}(n)-\Delta t}^{t_{\text{off}}(n)+\Delta t} R(t) I^2 \mathrm{d}t = - \lim_{\Delta t \to 0} \int_{t_{\text{off}}(n)-\Delta t}^{t_{\text{off}}(n)+\Delta t} LI \frac{\mathrm{d}I}{\mathrm{d}t} \mathrm{d}t\,, \tag{22b}$$

where the last integration of $\int LI \mathrm{d}I/\mathrm{d}t \times \mathrm{d}t = \int LI \mathrm{d}I$ becomes $-(L/2) I_{\text{off}}^2(n)$, $I_{\text{off}}(n)$ being the current right before the switching-off, $t_{\text{off}}(n) - \Delta t$. It means that the energy dissipation by the rapid rise in resistance can be calculated simply by $(L/2) I_{\text{off}}^2(n)$. In other words, all the electrical "kinetic energy" stored right before the switching-off is consumed by the huge resistor in order to reach $I = 0$. The energy integration over the whole time, shown in Eq. (21), is now divided into the Joule heating integration $\int R(t) I^2 \mathrm{d}t$ over the MOSFET-on periods with $R(t) = R_{\text{on}}$ and the energy consumed over all the sudden switching-off moments. Finally, all the energy integrations in Eq. (21) are also normalized by the incident sound energy E_{inc}, giving

$$\alpha_{\text{on}} = \frac{L_{\text{cav}}}{h_0^2 E_{\text{inc}}} \int_{g=1} R_{\text{on}} I^2 \mathrm{d}t\,, \qquad \alpha_{\text{off}} = \sum_n \frac{L}{2} I_{\text{off}}^2(n)\,, \qquad \alpha_x = \alpha_{\text{on}} + \alpha_{\text{off}}. \tag{22c}$$

The combination of the last equation of Eq. (22c) with Eq. (20) gives the grand total energy conservation in all fundamental physical elements

$$\alpha_{dm} + \alpha_{\text{on}} + \alpha_{\text{off}} + \beta + \gamma = 1. \tag{23}$$

Note that the integration for α_{on} is conducted over the MOSFET-on ($g = 1$) periods, but it can also be extended over the entire period since $I = 0$ is assigned for the MOSFET-off periods anyway. All the energy integrations can be calculated by the summation over all frequency components (according to Perceval's theorem) when the fluctuation signals are Fourier transformed except α_{off} which has to be added up from all individual switching moments. The spectral analysis is more revealing than the direct time-integration as we seek to study spectral scattering of sound energy.

For the typical examples presented in the next section with 100 time steps for the source oscillation cycle, the error for energy conservation in the mechanical part, Eq. (20), is 0.020%, while that for the electrical part, Eq. (22c), is 0.025%. The error for the total energy conservation in Eq. (23) is 0.004%, indicating mutual cancellation of errors. In addition to the above self-consistency check, the time-domain numerical simulation scheme was validated by experiment in our previous work on the normal incidence configuration, cf. Fig. 3(d) of [28].

3. Results for spectral scattering

Since there are many design variables, we limit ourselves to the set of parameters in Table 1. Note that all extensive diaphragm and shunt circuit properties, $m, d_m, \kappa, Bl, R_{\rm on}, C, L$, are given in terms of per diaphragm surface area equal to h_0^2 based on the test rig used in the experiment of [28] except that mechanical damping is given $d_m = 0$ as we use electrical resistor for system damping instead. For the diaphragm length used in most of the computations below, $L_{\rm cav} = 2h_0$, and with the lateral width of h_0, the actual diaphragm surface area becomes $2h_0^2$. The bulk properties, such as mass, should take the values twice the ones given in the table. The source frequency is $f_s = 150$ Hz for most figures except when the broadband incident noise source is studied in the last subsection.

Table 1. Parameters used for computations

Duct height	$h_0 = 0.1$ m	Cavity depth	$h_{\rm cav} = h_0$
Diaphragm length	$L_{\rm cav} = 2h_0$, except for Fig. 6		
Diaphragm mass	$m = 5.8$ g	Diaphragm spring constant	$\kappa = 4516$ N/m
Mechanical damping	$d_m = 0$	Diaphragm force factor	$Bl = 4.6$ Tm, except for Fig. 6 with 9.2 Tm
Capacitor	Absent, $C = \infty$	Inductance	$L = 0.2$ mH
Resistor	$R_{\rm on} = 0.05\Omega$, except when the effect of its variation is studied in Fig. 5		

3.1 Effect of modulation frequency

We first vary the modulation frequency f_m and subsequently look at the effect of the shunt resistor R. The variable to be minimized is the sound energy transmission to downstream, γ. It is recalled that, when a shunt-off design is equipped with the best damping according to Eq. (8), the minimal γ is obtained and is used as a reference, $\gamma_{\rm ref} = 0.75$, which is shown as the filled circle in Fig. 2(a). Results from all switching shunt designs will be compared with this reference.

The MOSFET switching is controlled by a gating voltage in experiment. In simulation, it is simpler to specify an oscillating function $y_m(t)$ which issues a switch-on command when y_m increases from negative to positive values, and a switch-off command when $y_m(t)$ decreases from positive to negative values. In this study, we choose the following function y_m, which is phase related to the incident wave pressure $p_{\rm inc}$ sensed at the diaphragm, $x = 0$,

$$p_{\rm inc}(0,t) = 1\ [\text{Pa}] \sin 2\pi f_s t\,, \qquad y_m(t) = \sin(2\pi f_m t - \theta)\,, \tag{24}$$

where θ is the phase delay. Note that when f_m is not a multiple of source frequency, $f_m \neq nf_s$, where $n = 1,2,\cdots$, θ has no meaning as the system goes through all values of θ, but θ will be consequential when $f_m = nf_s$, which will be investigated below. In actual implementation, it is possible to feed the voltage present in the coil, Blv, through a low-pass filter, and amplify the filtered signal to create the gating voltage. Since the gating voltage is merely used to operate MOSFET, it does not constitute a feedback loop that has the potential to destabilize the system.

Figure 3 shows the effect of f_m on the wave outputs, by absorption, reflection and transmission. The results are obtained by summing up contributions from all frequency components after the time-series are Fourier transformed. Figure 3(a) is for γ which has an obvious trough at $f_m = 2f_s = 300$ Hz. This double-frequency relation, with optimal $f_m/f_s = 2$, is found to be true through numerical simulations for a wide range of source signal of interest, $f_s \in (50,250)$, although we have not obtained an analytical proof for this. The trough value achieved is $\gamma = 0.65$, which is better (lower) than the reference, $\gamma_{\text{ref}} = 0.75$. The results at $f_m = f_s = 150$ Hz and $f_m = 2f_s = 300$ Hz depend on the phase angle θ and the

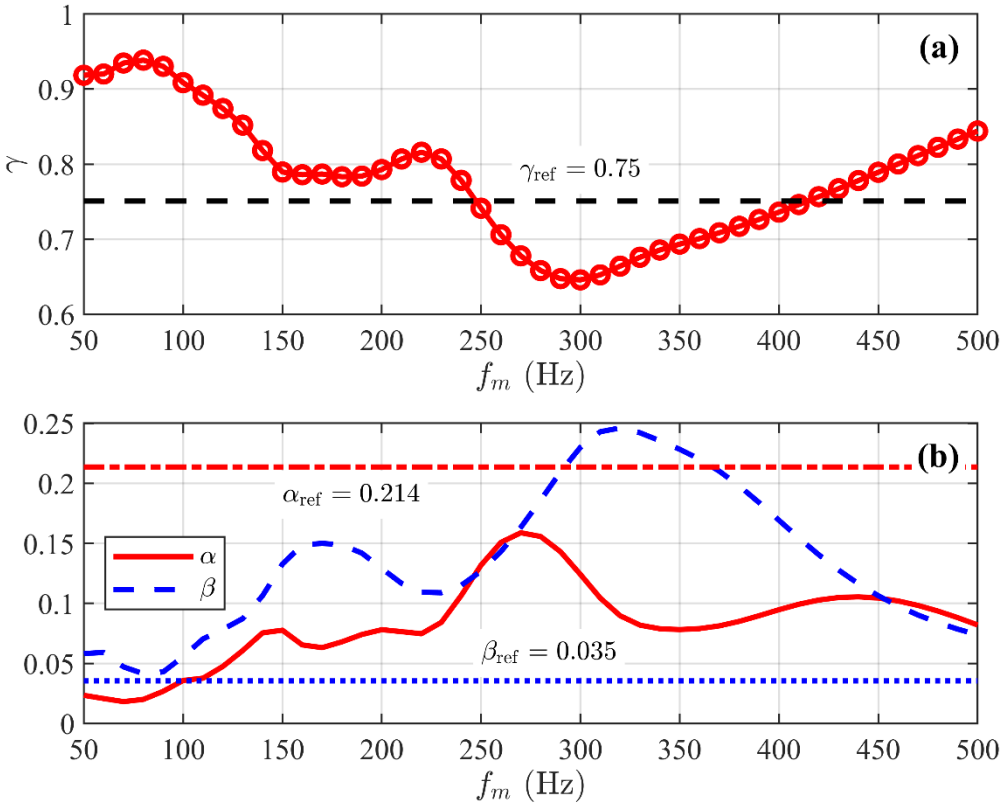

Figure 3. Variation with modulation (switching) frequency f_m and comparison with the reference results achieved by the optimal passive diaphragm, according to Eq. (8), shown as horizontal lines. (a) The transmission coefficient, which reaches a minimum of $\gamma_{\text{min}} = 0.65$ at $f_m = 2f_s = 300$ Hz. (b) Absorption (dashed line) and reflection coefficients.

result presented in Fig. 3(a) is averaged over all phases, $\theta \in (0,2\pi)$. The variation with respect to θ is analyzed in the next figure. Figure 3(b) shows the absorption (solid line, α) and reflection (dashed line, β) coefficients, both compared with the respective reference values drawn as horizontal lines with labels. For most f_m values covered in this figure, the absorption is well below the reference value of $\alpha_{\text{ref}} = 0.214$, but the reflection is well above the reference value of $\beta_{\text{ref}} = 0.035$. The results at $f_m = 300$ Hz do not show special features for the curves of α and β.

Since the results for $f_m = 2f_s$ are the most encouraging, we now focus on this case and explore the effect of θ, together with the setting of $f_m = f_s$. Figure 4(a) is for $f_m = f_s$, while Fig. 4(b) is for $f_m = 2f_s$. In terms of γ (solid curve with open circles), it is interesting to note that the lowest value for $f_m = f_s$ in Fig. 4(a) happens to be almost the same as the average value of γ for $f_m = 2f_s$, which is highlighted by a filled circle in Fig. 4(b) at $\theta/\pi = 1.04, \gamma = 0.65$. The trough of $\gamma = 0.38$ at $\theta = 1.56\pi$ is highlighted by another filled circle. Both phase settings will be analyzed below. The curves of the sound absorption α (thin solid lines) have phase shifts relative to the curves of the transmission coefficient γ, but the reflection curves β (dashed lines) are almost the exact opposite in phase with the

γ curves. Since reflection depends on the diaphragm vibration, it means that more diaphragm vibration is good for noise control at downstream.

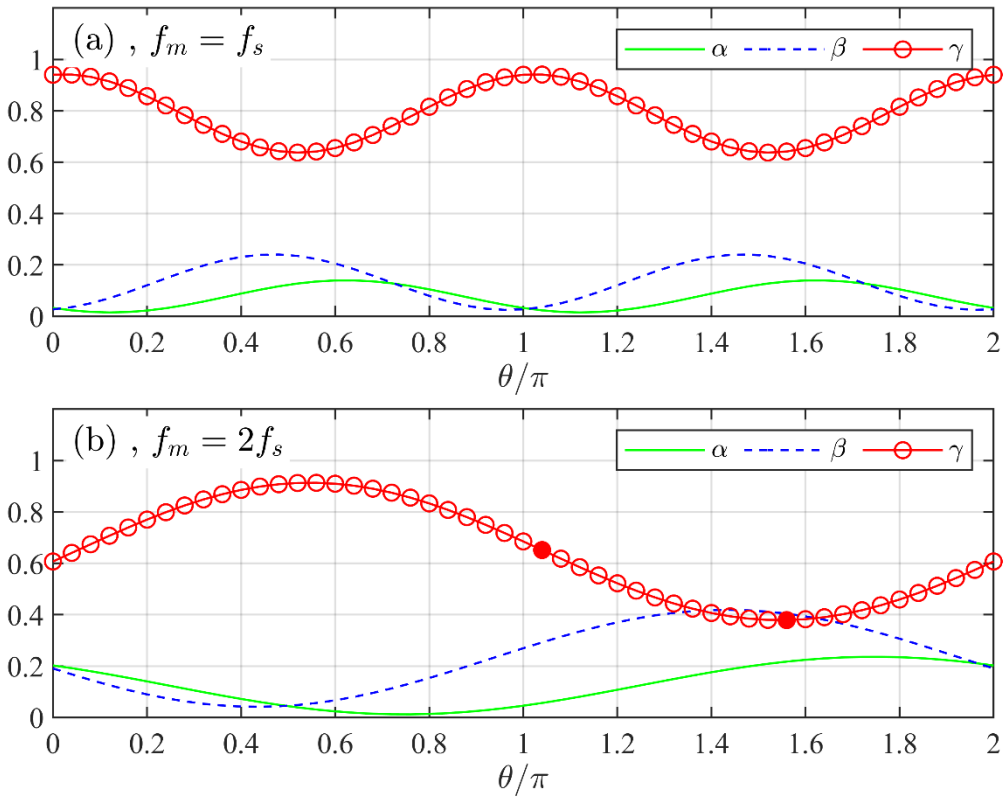

Figure 4. Sound absorption, reflection and transmission for (a) $f_m = f_s$, and (b) $f_m = 2f_s$ when the phase of the modulation varies relative to the source signal. The two filled circles in (b) represent, respectively, the average result for all the phases, and the minimum transmission coefficient.

With $f_m = 2f_s$ fixed, we are left with only two design variables, shunt circuit resistor R and MOSFET phase angle θ. A simple parametric scan produces the optimal design parameter shown in Fig. 5 for $f_m = 2f_s = 300$ Hz. Figure 5(a) shows a minimum transmission $\gamma_{\min} = 0.38$, which is about half of $\gamma_{\text{ref}} = 0.75$. This is achieved at the lowest resistor value scanned, $R = 0.05\Omega$. Figure 5(b) shows the same location for the peak reflection coefficient β, similar to the trend shown in Fig. 4(b). In Figure 5(c), the total sound absorption α includes mechanical damping, which is zero in this case as $d_m = 0$, the shunt-on Joule heating RI^2, as well as the switching absorption of $(L/2)I_{\text{off}}^2$, where I_{off} is the value of the current right before switching-off. Here, it is obvious that the design for $\gamma_{\min}$ is not achieved because of the maximum absorption, but rather a lowest value of α in the range studied. Note that the same is not quite true if the same study is conducted for $f_m = f_s$, where $\gamma_{\min}$ is found as a compromise between α and β, which have separate peak settings. Figure 5(d) shows the ratio of energy conversion in the system from the source frequency to all other frequencies, which in this case is simply $f = nf_s, n = 3,5,7,\cdots$. Since all energy components in Eq. (23) have spectral distribution, the ratio of the total energy scattering is defined as the sum of energy outside f_s,

$$\eta_{\text{conv}} = (\alpha_{dm} + \alpha_{\text{on}} + \alpha_{\text{off}} + \beta + \gamma)|_{f \neq f_s}. \tag{25}$$

When $\gamma_{\min}$ is achieved, the total conversion is $\eta_{\text{conv}} = 0.43$. If the percentage of non-source-frequency is calculated in the transmitted sound only, η_{conv} would be 0.37 (not shown).

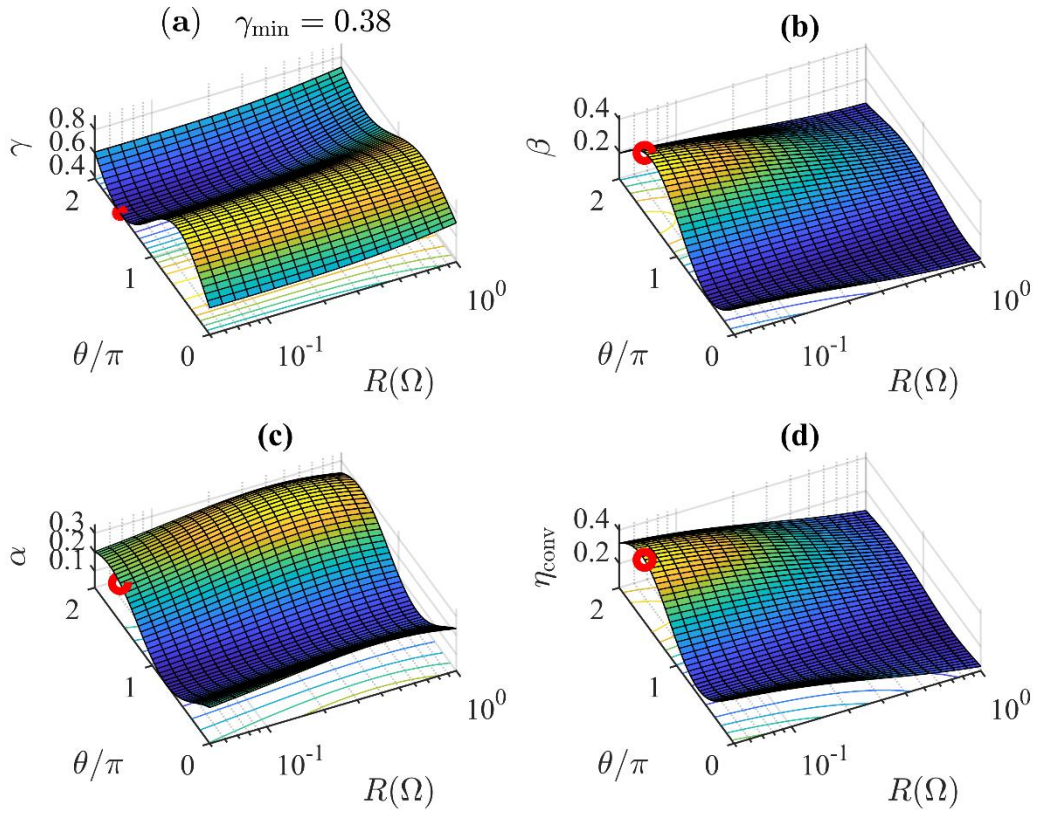

Figure 5. Effects of resistor R and phase for double-frequency modulation θ ($f_m = 2f_s = 300$Hz). (a) Surface plot of $\gamma(\theta, R)$ with the trough shown in red circle found at the minimum resistance $R = 0.05\Omega$ and $\theta = 1.56\pi, \gamma_{\min} = 0.38$. (b) Reflection coefficient β. (c) Absorption coefficient $\alpha = \alpha_{dm} + \alpha_{\text{on}} + \alpha_{\text{off}}$. (d) Total spectral scattering ratio in sound energy, η_{conv} defined in Eq. (25). The optimal point for $\gamma_{\min}$ is also marked by open circles in sub-figures (b), (c) and (d).

In Fig. 5, the results for (a) γ, (b) β, (c) α and (d) η_{conv} essentially show a rather separable influence of θ and R. While the variations with θ is periodical, as shown in Figs. 3 and 4, the same for R is monotonic for all except α where a peak of $\alpha = 0.34$ appears at $R = 0.39, \theta = 1.68\pi$. Note that the trough point for γ has $\theta = 1.56\pi$, and so the peak for α is only slightly shifted in terms of θ, as was shown clearly in Fig. 4 when the thin solid lines are compared with the thin dashed lines. The minimum of γ (0.38) is achieved at a relatively low α (0.22) but a high β (0.40) and a high η_{conv} (0.43). Later analysis (Fig. 9) shows that scattering has a key role in achieving the low transmission by suppressing the cavity acoustic reactance. The results in Fig. 5 allow us to fix $R = 0.05\Omega$ for subsequent studies with the geometry of $L_{\text{cav}} = 2h_0$. The theoretical optimum should be $R = 0$ but it is not realistic. Besides, the results are very similar.

The level of transmission loss (TL) achieved by the best result in Fig. 5(a), $\gamma_{\min} = 0.38$, is TL $= -10 \lg 0.38 = 4.2$ dB, which may not seem signficant. The performance of the device is now examined together with the standard duct lining occupying the same cavity volume of $h_{\text{cav}} \times L_{\text{cav}}$, cf. Fig. 1(c). When $h_{\text{cav}} = h_0$ is fixed, the lining length L_{cav} determines the volume. Figure 6 shows the monotonous increase of TL with L_{cav} for all four curves detailed as follows. Curve 1 is the performance of the current switching shunt design operated at a modulation frequency of $f_m = 2f_s$ and with the best phase angle (for each L_{cav} setting), as illustrated in Fig. 4(b). Curve 2 is for the average performance for $\theta \in (0, 2\pi)$. Curve 3 is for a cavity of length L_{cav} filled with fibrous porous material of flow resistivity 10,000 Pa $\cdot$ s/m^2, for which the equivalent fluid formulas of Miki [33] have been adopted in a Comsol® simulation with the downstream boundary allowing all waves to exit the computational domain. Curve 4 is obtained when the cavity is empty, serving as a purely reactive expansion chamber. The gaps between curve 3

and curves 1 and 2 demonstrate the beneficial effects of spectral scattering. Please note that Bl values for curves 1 and 2 have been set as twice as much as that adopted for Figs. 2-5, but other diaphragm parameters have remained the same. Please also note that as L_{cav} increases further, the compact-device assumption, $L_{\text{cav}} \ll \lambda$, where λ is the wavelength, implicit in Eqs. (2,3,6) may fail for curves 1 and 2. A practical workaround for $L_{\text{cav}} = 8h_0$ is the following. Instead of using a single diaphragm covering a single cavity of length $8h_0$, a square duct with 4 identical diaphragms and cavities of $2h_0$ are attached to the four duct sides. When higher TL is desired, which is entirely possible with more volume, multiple units are needed along the duct and the none-compactness needs to be taken into account by simultaneously solving for the vibration velocity of all diaphragms in series.

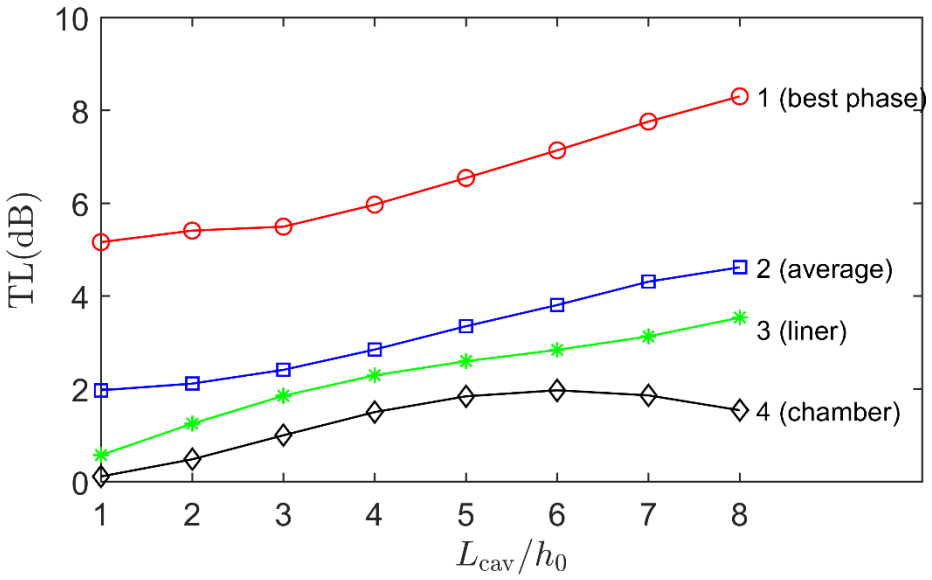

Figure 6. Improvement of device performance with the total volume occupied by the cavity. The cavity depth for all configurations shown here is $h_{\text{cav}} = h_0$, while the cavity length L_{cav} varies. Curves 1 and 2 are for the switching shunt design, in which the properties of the diaphragm per unit surface area h_0^2 are listed in Table 1, except that the magnetic force factor is doubled, $Bl = 9.2$ Tm. Curve 1 is the result using the best phase θ for the gating voltage expressed in Eq. (24), while curve 2 is with the average performance derived for $\theta \in (0,2\pi)$. The duct liner for curve 3 has a cavity filled with a fibrous porous material of flow resistivity 10,000 Pa $\cdot$ s/m^2 using the Miki [33] equivalent fluid model. Curve 4 is the performance of empty cavity forming an expansion chamber.

3.2 Details of spectral scattering mechanism

Figure 7 shows the waveforms of the optimal modulation identified in Fig. 5(a) by the open circle, with $f_m = 2f_s = 300$ Hz and $\theta = 1.56\pi$. Figure 7(a) compares the incident wave (dashed line) with the transmitted wave (solid line), both measured at the diaphragm position. Since $\gamma = 0.38$, the r.m.s. amplitude of the transmitted wave has an amplitude of $\sqrt{\gamma} = 62\%$ times that of the incident wave. Figure 7(b) shows that switching-off occurs twice in the source wave cycle and it does not quite happen when the current I reaches its peak magnitude. The peak Lorentz force is more than twice the force of the incident wave acting on the cross section of h_0^2, or roughly equal to the incident wave force on the entire diaphragm surface with length $L_{\text{cav}} = 2h_0$. Despite the appearance of not dumping the electrical energy at the peak current magnitude, the amount of system energy consumed by the switching-off

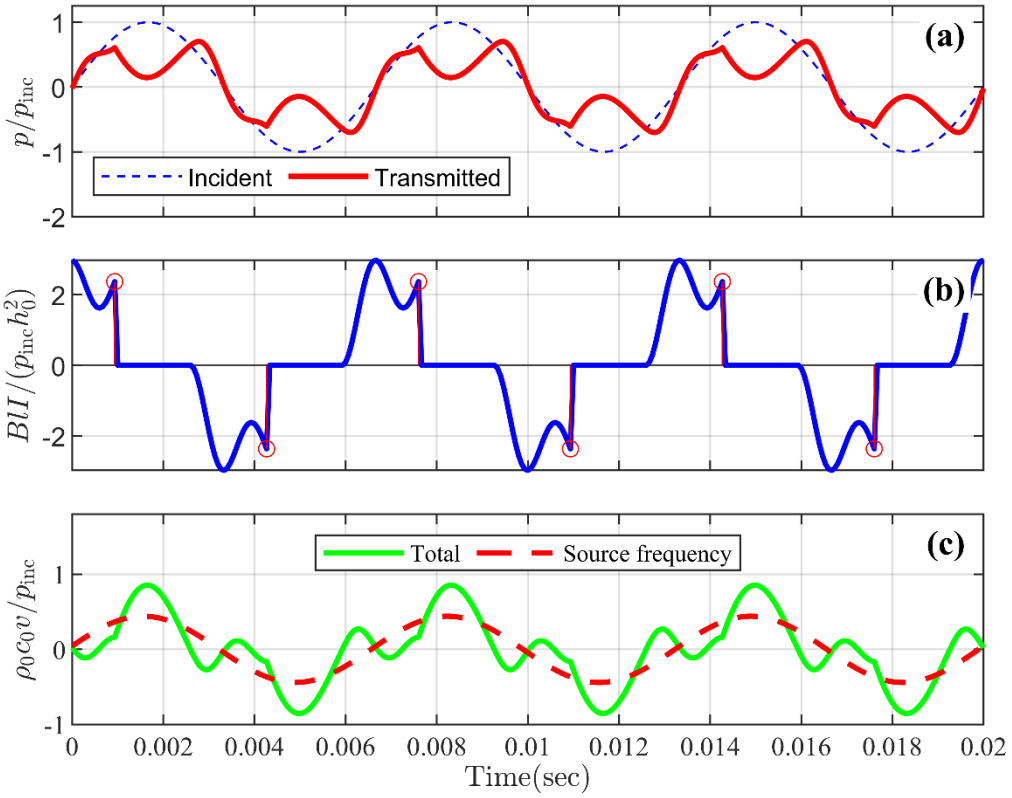

Figure 7. Time-domain result for the double source-frequency modulation ($f_m = 2f_s = 300$ Hz). (a) Incident and transmission wave compared. (b) Shunt circuit current I shown in the normalized form of $BlI/(p_{\mathrm{inc}}h_0^2)$, with open-circle indicating the exact moment of switching-off. (c) Diaphragm vibration velocity (solid line) with the source frequency component (dashed line) plotted for phase reference. All coordinates are shown in normalized form indicated by the vertical axis labels. The time coordinate $t = 0$ here is 0.1 sec, or 15 cycles, after the incident wave is launched and when the waveforms have become stationary.

action, α_{off} defined in Eq. 22(b), has the lion share of 98.5% of the total electrical energy drained, $\alpha_{\mathrm{on}} + \alpha_{\mathrm{off}}$. When the energy is consumed gradually by the shunt-on resistor R_{on}, one can expect the same behaviour of energy dissipation as that by mechanical damping. It is well known that such damping induces phase differences in the vibration response and hence waveform distortion when the incident wave is not of a single frequency. For the current modulation design, however, damping almost exclusively occurs all of a sudden by the MOSFET switching. This changes the phase response of the diaphragm in relation to the incident wave forcing. Moreover, the phase relation is adjustable, instead of being fixed with vibration velocity in a traditional mechanical system. The implication of this will be analyzed further below when the equivalent acoustic impedance introduced by the modulating device is examined.

The diaphragm vibration velocity v is shown in Fig. 7(c) (solid line) in a form normalized by the acoustic particle velocity $p_{\mathrm{inc}}/(\rho_0 c_0)$. The component of v for the source frequency f_s (dashed line) is also plotted for examining the phase angle relation with the current I in Fig. 7(b). It is observed here that the vibration is particularly rigorous when the circuit is switched off, namely in the time segment with the flat line of $I = 0$ in Fig. 7(b). This is so because the diaphragm has zero mechanical damping and is therefore responding to the incident wave well. During the shunt-on period, the vibration is subdued due to the fact that a small resistor of $R = 0.005\ \Omega$ almost constitutes a short circuit, which presents a huge induced acoustic impedance forbidding the vibration. It is such drastic change between the damping-free responses to almost an on-hold state of the diaphragm that scatters the frequency

content of the incident wave. The current is at a high amplitude when the circuit is switched off, dumping all the electric energy stored in the electric spring, the inductor, to the huge resistor present in MOSFET at the switch-off position. The amount of energy damping created will also be analyzed in the form of acoustic impedance further below.

Figure 8 shows the spectra for the transmitted wave and electro-mechanical coupling defined below for the two phase-settings identified in Fig. 4(b) by the filled circles. One is the best performance with $\theta = 1.56\pi$, shown here in sub-figures (a) and (c), and another is the average performance with $\theta = 1.04\pi$ in sub-figures (b) and (d). All sub-figures have double y-axis. The right-hand side is for the cumulative energy shown in thin solid curves, normalized by its own maximum. Cumulative energy is particularly helpful in spectral analysis as it visualizes the actual energy contribution when the system response is spread over a frequency band and the height of discrete peaks can be misleading, especially when presented in the decibel scale. The solid curve in Fig. 8(a) is for the transmitted wave spectrum, calculated by $20\lg|p_t/p_{\text{inc}}|$. We see energy scattering to all higher-order frequencies of $f_s + nf_m, n \geq 1$. The cummulative energy curve, $\int |p_t|^2 \, \mathrm{d}f$, normalized by its own total, shows a dominant rise at the source frequency f_s, followed by a significant rise at the next peak of $f_s + f_m = 450$ Hz, and much less contributions from higher harmonics. If the energy outside the source frequency, $f \neq f_s$, is added up, it contributes 45% of the total transmitted wave. The total scattering ratio defined in Eq. (25) is $\eta_{\text{conv}} = 48\%$. The latter is more indicative of the effectiveness of spectral scattering as the transmission wave only accounts for $\gamma = 38\%$ of the incident wave energy in this case.

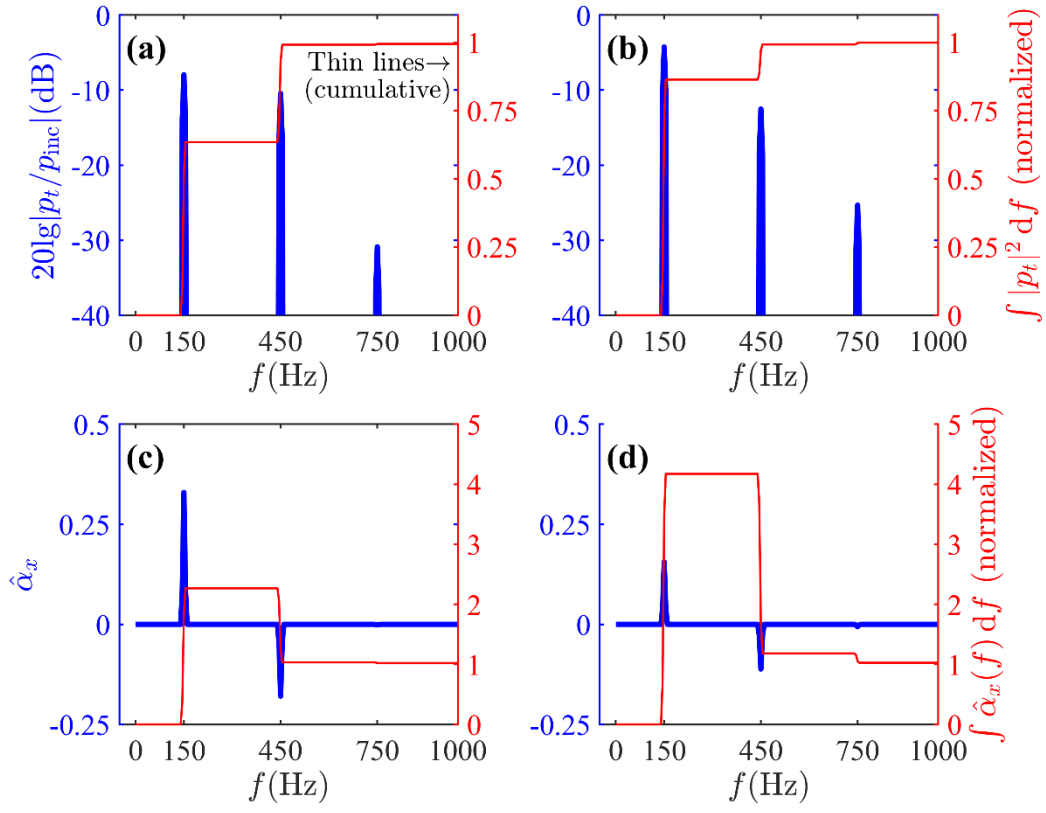

Figure 8. Spectral scattering analysis for the double-frequency modulation ($f_m = 2f_s$) for the two phase settings of best performance, (a) and (c), and average performance, (b) and (d), identified by the two filled circles in Fig. 4(b), $\theta = 1.56\pi, 1.04\pi$, respectively. As illustrated in sub-figure (a) but applicable to all sub-figures, the thin solid lines are the cumulative spectra for the thick solid curves in each sub-figure corresponding to the right coordinate axes. (a) and (b) are for the transmitted wave spectra while (c) and (d) are for the electro-mechanical coupling spectra.

Figure 8(b) is for the average-performance setting, for which the energy in the scattered frequencies is less than that in Fig. 8(a). Figure 8(c) shows the cross-correlation spectrum for the Lorentz force BlI and the diaphragm vibration velocity v. The result is normalized by the incident wave energy E_{inc},

$$\hat{\alpha}_x(f) = \frac{L_{\text{cav}}Bl}{2E_{\text{inc}}h_0^2}\,\text{Re}\left(\hat{I}\hat{v}^*\right), \tag{26}$$

where $\hat{I}$ and $\hat{v}$ are, respectively, the Fourier transforms of the current and vibration velocity, and superscript '*' denotes complex conjugate. The sum of the coupling coefficient $\hat{\alpha}_x(f)$ over all frequencies is simply α_x defined in Eq. (19). The coupling spectrum in Fig. 8(c) shows a prominent peak at f_s, as expected, but it becomes negative at all sum frequencies. Negative value implies that, without energy input, there is energy output to the diaphragm vibration as well as energy damping occurring at higher frequencies. This is the direct evidence of spectral scattering. The sum of the positive and negative coupling coefficients over all frequencies is equal to the sum of energy damping in the circuit, $\alpha_{\text{on}} + \alpha_{\text{off}}$, which is guranteed by the stationary process governed by the circuit equation (11). The cumulative sum shown in Fig. 8(c) eventually comes down to unity as it is normalized by its own total. The amount of over-shoot at f_s, or the depth of the dive at 450Hz, indicates the extent to which the spectral energy is scattered. Figure 8(d) shows that the coupling is weaker even at f_s when compared with Fig. 8(c).

The above analysis concerns either time-domain events or spectral scattering in terms of the quantitative outcome. The mechanism is now further analyzed from a new perspective. Suppose the spectral scattering is an additional material property that changes the device response to the source frequency f_s, knowing that the radiation of sound at the scattered frequencies is entirely separate. We now focus on the change of device response to the source frequency and compare it to the non-switching configurations, either without a shunt circuit, or with a shunt circuit constantly engaged. The device impedance of the latter is given in Eq. (4) as the interface impedance. When switching occurs, the new impedance is now calculated by the actual waves transmitted according to Eq. (6). Given the complex value of p_t/p_{inc}, we work backwards from Eq. (6) to obtain the equivalent interface impedance denoted here as Z'_{int},

$$Z'_{\text{int}} = Z_{\text{rad}}\frac{p_t/p_{\text{inc}}}{1 - p_t/p_{\text{inc}}}, \tag{27}$$

where the real-valued radiation impedance, $Z_{\text{rad}} = L_{\text{cav}}/(2h_0)$, remains unchanged. This impedance Z'_{int} is compared with the effective impedance when the shunt-on and shunt-off each taking half of the online time-share, which may be called the multiplexing arrangement. Since the exact timing of the shunt-on and shunt-off is different, the wave output from each will have a different phase angle. When the switching takes place at a frequency unrelated to the source signal, this phase angle sweeps through all values and the interference effect vanishes over a long period of Fourier transform integration. The result is equivalent to a fully fused combination of time-share in which the switching between them occurs so frequently that they are present in parallel "time-channel" each taking half of the total time. When switching is synchronized with the source signal, this is no longer the case. The phase will have a serious impact on the results, as was revealed in Figs. 4 and 5. Nevertheless, we shall still define a "neutral" state of multiplexing in which the two are fully fused, and assign the effects of timing as part of the temporal scattering that mainly arises at the instants of switching. Mathematically, temporal scattering is defined as the difference between the actual wave output from the system and an ideal, fully fused multiplexing state described above. In a time-constant system, spatial singularity can scatter waves from one wavenumber to another, and so is temporal scattering which scatters wave energy from one frequency to another. Since the transmission wave in the fully fused multiplexing case is simply the average of the two states, we define the impedance of spectral scattering ΔZ_{sc} as follows,

$$p_t' = \frac{1}{2}(p_t|_{\text{shunt on}} + p_t|_{\text{shunt off}}), \qquad Z_{\text{mpx}} = Z_{\text{rad}} \frac{p_t'/p_{\text{inc}}}{1 - p_t'/p_{\text{inc}}}, \qquad \Delta Z_{\text{sc}} = Z_{\text{int}}' - Z_{\text{mpx}}. \quad (28)$$

Here subscripts 'mpx' and 'sc' denote multiplexing and scattering, respectively.

Figure 9(a) compares the complex transmission ratio p_t/p_{inc} for shunt-off (open circle), shunt-on (cross), fully fused multiplexing (open square) and the switching shunt (diamond) in the complex plane. This is for the double-frequency modulation identified as the average design point, $\theta = 1.04\pi$, in Fig. 4(b). Surely, the multiplexing transmission lies in the middle between the shunt-on and shunt-off states, but the switching shunt (diamond) is distinctively different. All symbols are connected to the origin for clarity. Figure 9(b) is the complex-plane presentation for the four impedances. The shunt-off impedance is -3.5i, in which the mechanical spring contributes -0.83i and the cavity contributes -2.65i. The shunt-on impedance is $6.6 - 28$i which has a huge magnitude stretching to the right-lower corner in Fig. 9(b). This is mainly due to the small resistance and inductance used. When combined in parallel, the

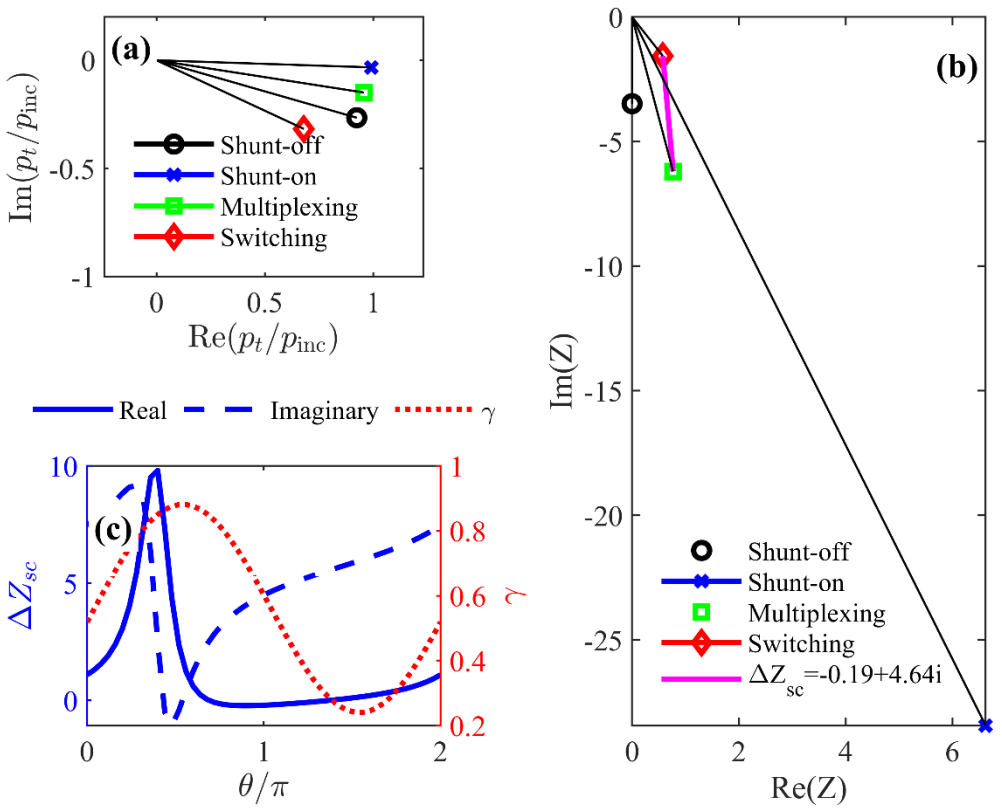

Figure 9. Equivalent impedance analysis for the switching shunt compared with the shunt-off, shunt-on and the multiplexing state. The latter refers to the equal time-share between the shunt-on and shunt-off conditions according to the switching function given in Eq. (24), without accounting for the scattering effects. (a) Complex transmitted wave amplitude. (b) Variation of scattering induced impedance with phase angle θ. (c) Complex-plane presentation for the scattering and other impedances. The design setting is the average-performance point with $f_m = 2f_s, \theta = 1.04\pi$ (the left filled circle in Fig. 4(b)).

multiplexing impedance is more moderate, $0.77 - 6.2$i. It is noted that the stiffness is still higher than the shunt-off configuration, but the available damping (real part, 0.77) is inadequate, recalling that the optimal damping for the shunt-off design is 3.01. The switching configuration has a drastically different impedance of $0.58 - 1.56$i. The reactive part is so small that the damping, 0.58, is about half of the optimal damping 1.14 calculated from Eq. (8). The line drawn from the multiplexing impedance (open-square) to the switching shunt impedance (diamond) represents the scattering effect, $\Delta Z_{\text{sc}} = -0.19 +$

4.64i. Figure 9(c) gives the variation of the real (solid line) and imaginary (dashed line) parts of $\Delta Z_{\rm sc}$ with θ, together with the energy transmission coefficient γ (dotted line). The impedance lines are unremarkable around the troughs of γ, but there is a rapid rise near $\theta = \pi/2$ when the performance is poor, poorer than the pure shunt-off configuration. When the best performance point ($\theta = 1.56\pi$) is analyzed, the scattering impedance is found to be $\Delta Z_{\rm sc} = 0.16 + 6.0{\rm i}$. The switching shunt impedance itself is $0.93 - 0.20{\rm i}$ which is very close to the no-stiffness state or resonance. As a result, much more sound reflection occurs ($\beta = 0.40$) and much reduced transmission ($\gamma = 0.38$) is obtained. Although the reactance reduction of 6.0i by the optimally phased switching shunt is even higher than that of the passive device itself, $-3.5{\rm i}$, it is still slightly smaller than the 'multiplexing' state, which has $-6.2{\rm i}$. Figure 9(b) visualizes various impedance components.

The reason why the switching reduces the system reactance at the source frequency may be further explained by examining the phase relation between switching and the source frequency vibration, denoted here as $v_{fs}(t)$ and identified as the dashed line in Fig. 7(c). Switching occurs roughly when $v_{fs}(t)$ reaches its maximum magnitude. Sudden switch-off drains the maximum energy stored in the circuit by the MOSFET resistor. Since the Lorentz force opposes the coil motion in general, the sudden disappearance of the Lorentz force implies a relative boost for the diaphragm motion. The actual amount of boost depends on the coupling between the Lorentz force release and the vibration velocity. When the force and velocity are in phase, the enhancement is the greatest. Enhanced motion implies less restriction by the cavity stiffness. If the magnitude of v_{fs} is plotted as a function of switching phase, as is done in Figs. 4(a) and 4(b) in dashed lines, we find it to trend in the opposite direction with γ (the dashed line with open circle). In other words, when the magnitude of v_{fs} is high, the transmission is low, mainly because the system reactance reduction is large. Of course, the details of all the factors determining γ are complex, such as the resistance, the spectral spread of the energy, but we argue that the system reactance reduction by the sudden release of the reactive Lorentz force to be the crucial part of the spectral scattering mechanism.

3.3 Finite-band random noise as incident wave

The purpose of avoiding low-frequency resonance in the basic mechanical design of the diaphragm and in the circuit design is to make sure that the new mechanism of spectral scattering does not rely on narrow-banded resonance. It is also the reason why we analyze both the average-performance point in addition to the optimal point in Fig. 4 since the latter depends on phase and is a type of semi-active control. To achieve broadband noise control in a passive manner, it is necessary to test the conclusion derived from the single source frequency ($f_s = 150$ Hz) by broadband simulations. For this purpose, we start from a white noise, band filter it to $f_s \in (125{,}180)$Hz, which is roughly half of an octave around 150 Hz. The modulation signal is the single-frequency twice the centre frequency, $f_m = 300$Hz. The results are shown in Fig. 10. Figure 10(a) shows the band-limited source spectrum labelled as SPL_0 in decibels. The source frequency band and the first scattered frequency band, or the sum frequency band, $f_m + f_s \in (425{,}480)$ are marked by vertical grid lines. Figure 10(b) shows the cumulative sound reflection coefficients, $\int \beta df$, for the optimal passive design (reference) in dashed line and the switching shunt design in solid line. The legend also displays the total sound reflection coefficients ($\sum\beta$) for the entire frequency range, 0.037 and 0.195, for the reference and switching shunt designs, respectively. Figure 10(c) is for the transmitted wave, also in cumulative spectra. The reference case has $\gamma_{\rm ref} = 0.743$, which is almost identical to the earlier result of 0.75 for the single source frequency. The switching shunt (solid line) has $\gamma_{\rm sw} = 0.691$. The dominant transmitted sound lies in the source frequency region. However, the diaphragm vibration in the scattered frequency region, $(435{,}480)$ Hz, has a certain sound energy. This is much easier to absorb than the source frequency. So, if the device is used in conjunction with a traditional liner, be it porous-material-based or with some MPP design, this part of the energy may be excluded. Under such consideration, a dotted line is added for this outcome and the revised total transmission becomes $\gamma_{\rm sw+liner} = 0.624$. Figure 10(d) is the cumulative sound

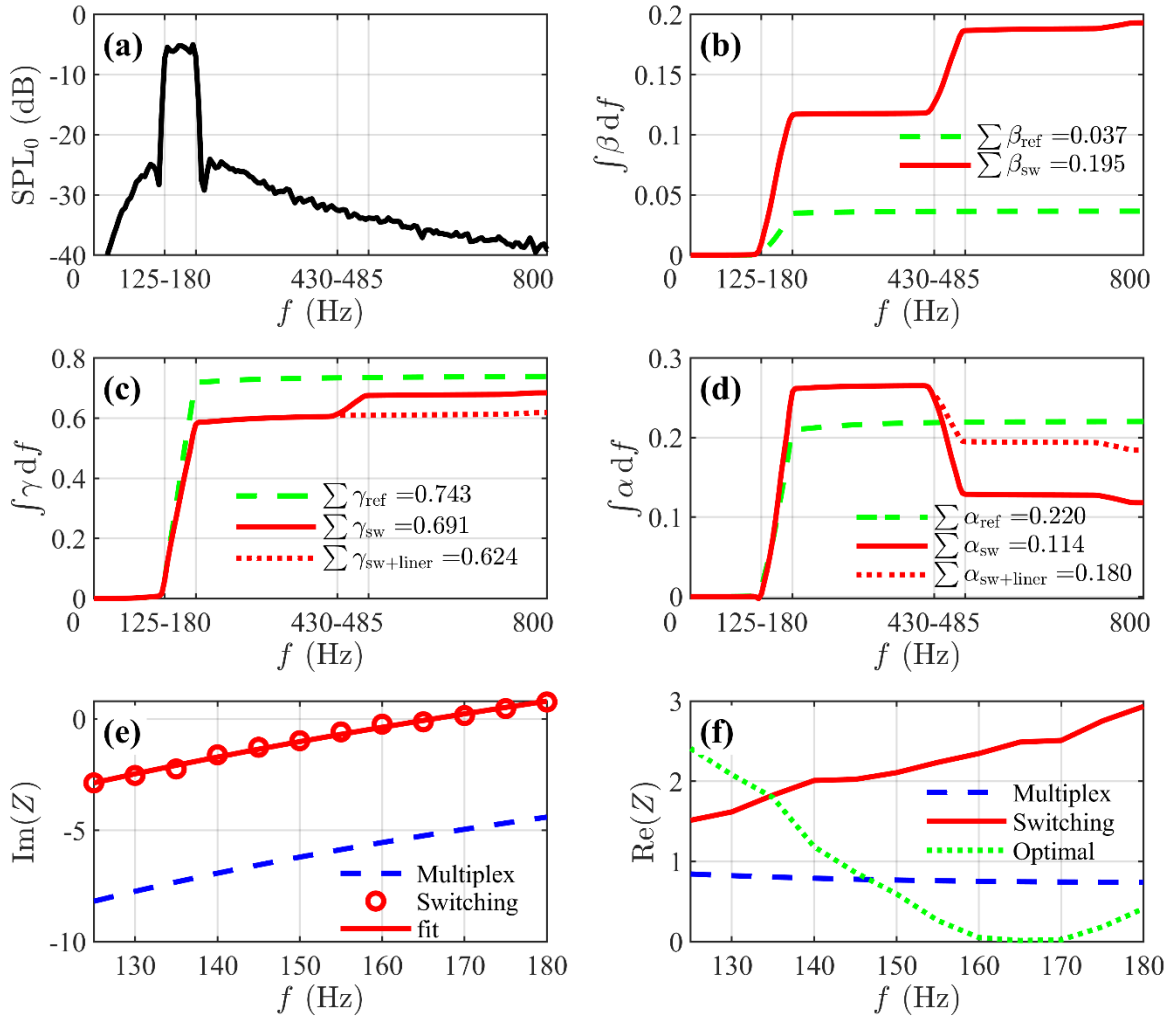

Figure 10. Finite-band spectral scattering and its comparison with the optimal shunt-off design. (a) The source spectrum with energy spread in the band of (125,180) Hz. (b) Cumulative sound reflection coefficient with the dominant content in the source region and significant energy in the sum frequency region of (430,485) Hz. The solid curve is for the switching shunt design while the dashed line is the reference design. (c) Sound transmission with a composite design (dotted line) added to exclude the sound scattered in the sum frequency. (d) Sound absorption. (e) Imaginary (reactive) part of impedance for the multiplexing (dashed line) and the switching shunt design (open circles) with least squares fit by $m\omega - \kappa/\omega$ in solid line. (f) Real (damping) part of impedance for the multiplexing setting (dashed line), the switching shunt design (solid line), and the optimal damping (dotted line) calculated by Eq. 8 using the actual system reactance shown in the open-circles in (e).

absorption spectra. Here, the scattered frequency region sees a decrease in the cumulative energy curve. This is so because there is no source energy in this region and any energy appearance in this region is counted as "negative absorption". The reference case has $\alpha_{\text{ref}} = 0.22$, the switching shunt has $\alpha_{\text{sw}} = 0.114$, and the switching shunt plus liner design has $\alpha_{\text{sw+liner}} = 0.18$. The switching shunt has a lower absorption due to the presence of the scattered frequency in the transmission. Comparing the total transmission of the switching shunt, $\gamma_{\text{sw}} = 0.691$, with the average performance of $\gamma = 0.65$ shown in Fig. 4(b), the broadband result is deteriorated by a moderate margin but the general improvement over the reference case still holds.

Figures 10(e) and 10(f) compare the multiplexing impedance calculated by Eq. (28) and the true interface impedance calculated by Eq. (27) for $f_s \in (125,180)$ Hz. Figure 10(e) deals with the

reactance part of the impedance, while Fig. 10(f) deals with the real part. For an electro-mechanical system, mass and stiffness can be frequency-dependent. It is somewhat arbitrary to assign a positive reactance to a positive mass or negative stiffness at a single frequency. The sign changes around resonance, and the seemingly new physics of negativity does not carry much impact on finite-band wave propagation. This issue can be settled by demanding the right frequency dependency of reactance over a finite frequency band. The logical step to take is to apply a least squares fit to the reactance curve by a system with constant mass and constant stiffness, $X \equiv \mathrm{Im}(Z) = m\omega - \kappa/\omega$. The open-circles in Fig. 10(e) are the samples of reactance over the frequency range of interest, $\omega_n, n = 1,2,3,\cdots N$. The collection of the discrete angular frequencies forms a column vector, so is the reactance. The least-squares fit is thus derived from the following method of pseudo-inversion of non-square matrix, which is based on the singular value decomposition using the matlab® function of "pinv",

$$\mathbf{X} = \begin{bmatrix} \mathrm{Im}\big(Z(\omega_1)\big) \\ \vdots \\ \mathrm{Im}\big(Z(\omega_N)\big) \end{bmatrix} = \underbrace{\begin{bmatrix} \omega_1 & \omega_1^{-1} \\ \vdots & \vdots \\ \omega_N & \omega_N^{-1} \end{bmatrix}}_{\mathbf{M}_{\boldsymbol{\omega}}} \begin{bmatrix} m \\ -\kappa \end{bmatrix}, \qquad \begin{bmatrix} m \\ -\kappa \end{bmatrix} = \mathbf{M}_{\boldsymbol{\omega}}^{+}\mathbf{X}. \tag{29}$$

Here, $\mathbf{M}_{\boldsymbol{\omega}}^{+}$ is the pseudo-inverse of the $N \times 2$ matrix $\mathbf{M}_{\boldsymbol{\omega}}$. The dashed line in Fig. 10(e) is for the multiplexing result, while the solid line through the open-circles is the least squares fit for the switching shunt. The values for mass and stiffness in this frequency range are given in Table 2. Obviously, the shunt-off state has exactly the right diaphragm mass and suspension stiffness plus cavity stiffness calculated by Eq. 4(b). The shunt-on state has a strange combination of large stiffness and marginally negative mass. This is caused by the phase distortion in the series electrical circuit. The electro-magnetically induced acoustic impedance is given in Eq. (4a) as $(Bl)^2/Z_e$. Therefore, the series circuit acts on acoustic admittance in a serial manner. It is therefore harder to interpret the results in terms of acoustic impedance. As shown in Table 2, the multiplexing system mass (9.16g) is much higher than the diaphragm (5.80g), and the system stiffness (32.67 kN/m) is much higher than the shunt-off (18.93 kN/m). What really counts is the switching shunt results, which has a mass of 20.05 g and a stiffness of 21.83 kN/m. The conclusion is that the system stiffness is increased by a small margin with respect to the shunt-off state, but the effective diaphragm mass is increased significantly. The mass increase is so significant that the system actually reaches resonance ($\mathrm{Im}(Z) = 0$) around 165 Hz. In other words, spectral scattering essentially adds to the system mass which counters cavity stiffness in the low-frequency region. This outcome contrasts with the negative stiffness envisaged by Huang [29] and experimentally demonstrated by Chiu et al. [34] in which a magnetized diaphragm is attracted by a permanent magnet in the cavity.

Table 2. Least-squares fit for the system mass and stiffness over the frequency range of (125,185) Hz

State	Shunt-off	Shunt-on	Multiplexing	Switching
Mass m (gram)	5.80	-1.55	9.16	20.05
Stiffness κ (kN/m)	18.93	110.92	32.67	21.83

Figure 10(f) shows the real parts of the impedances, or damping. It is found that the switching shunt design (solid curve) has a higher damping than the multiplexing setting (dashed line); the latter is essentially a constant. The dotted line is the optimal damping corresponding to the actual reactance to achieve the minimal wave transmission, which is calculated by Eq. (8) with the reactance shown in the open-circles in Fig. 10(e). The optimal damping is zero when the system resonates around 165 Hz. At all other frequencies, the actual system damping (solid line) does not follow the optimal damping. It means that the system design using such a few degrees of freedom cannot suppress wave transmission over a finite bandwidth. The outcome of spectral scattering is quite similar to the parallel arrangement of resonators in normal incidence [17], for which the essential physics is recalled below. When two resonators are in space parallel and they have a small difference in impedance properties, namely when

their resonance peaks are close to each other, the decoupled response of resonators produces different velocity responses. This difference produces radiation pressure difference that induces an internal flow between resonators to balance the pressures; the resonators are then coupled. The coupling has two effects: one is to increase the system damping as extra flux is introduced, and the other is to increase system inertia due to the same extra acoustic particle velocity. For the case of temporal scattering discussed in the current study, the tendency for the diaphragm to continue vibrating with the pattern of motion set up by one state of shunt is not cancelled by the sudden switching of MOSFET. Instead, the old motion presents itself as an extra system inertia for the new shunt state. This is also similar to the virtual mass in a fibrous material when air particles oscillate and have to change directions constantly due to the random fiber arrangement. The fact that temporal scattering brings positive system mass instead of negative system stiffness means that the performance enhancement in a finite-band is frequency dependent and further broadening of the source frequency, (125,180) Hz in the current example, will cause gradual deterioration of the performance gain by the scattering. A truly broadband reactance reduction remains the ideal design goal of acoustic metamaterial to be further explored.

4. Conclusions

We have chosen a stiffness-dominated side-branch absorber as the basis for study. When the optimal damping corresponding to the large reactance is selected, the energy ratio of the transmission is found to be 75%. This is reduced to 65% by switching shunt design when the modulation frequency is twice the source frequency without phase synchronization. When the latter is applied, the transmission ratio is reduced to 38%. The finite-band sound source is tested with the same method and is found to yield 69% in energy transmission, not as good as the single frequency but still shows promise. For a truly broadband sound source, it is expected that the side-branch can be divided into multiple segments, each catering for a finite bandwidth. Extensive further parametric studies will be needed for such a design.

Focusing on the fundamental mechanisms of the switching shunt, the following observations are made.

(1) When a shunt circuit is suddenly switched off, the energy of the diaphragm vibration is stored in the form of electrical energy and is consumed by the large MOSFET resistance instantaneously. This constitutes a new form of damping that is very different from the usual mechanical damping; the latter is incremental over time and is phase locked with the vibration velocity.

(2) It is found that, when the modulation signal is synchronized with the incident sound source, the impact of switching is phase dependent and presents opportunity for optimization. The phase of the shunt switching is programmable and it could be used to achieve a very different effect in addition to the sound energy extraction. On the other hand, a modulation frequency unrelated to the source frequency does not have meaningful phase, and the result is similar to the modulation at the multiples of the source frequency but with phase angle varying between 0 and 2π. The latter presents itself as a kind of "average" performance that is much easier to implement and achieve. In the examples given, the average performance can still be better than the shunt-off design with optimized parameters and offer a rather realistic prospect of a truly passive design.

(3) For a stiffness-dominated side-branch, the crucial element in wave manipulation is the reduction of equivalent system reactance seen by the incident wave. The sudden switch-off releases the Lorentz force that normally opposes the diaphragm motion. The removal of the Lorentz force represents a boost to the diaphragm motion, which is otherwise stifled by the cavity stiffness. Maximum boost is achieved when the switching is synchronized with the diaphragm vibration velocity. Temporal or spectral scattering is found to completely neutralize the reactance of the system. Detailed analysis reveals that the reactance reduction is a result of extra system mass introduced by the scattering instead of direct stiffness reduction, in a way similar to the space parallel arrangement of resonators.

(4) The scattering caused by the switching shunt appears to be the strongest when the mechanical and electrical systems are both close to damping-free states. When the resistor in the shunt circuit is small, close to a short circuit, the electromagnetically induced acoustic damping is very large, so is the equivalent system stiffness. The mechanical system response transits between a damping-free vibration to one that has a very high damping and stiffness. The total energy scattering defined in Eq. (25) is found to be as high as 43%, for the optimally synchronized modulation design. In terms of the reduction of the transmitted waves, the major contribution is derived from enhanced wave reflection.

Acknowledgements: the work is supported by a general research fund project 17210720 of the Research Grants Council of HK SAR Government, and a National Natural Science Foundation of China, Project No. 52105090. The article is written to honour the first author's PhD supervisor, Professor Shôn Ffowcs Williams.

References

[1] A. Selamet, I.J. Lee, N.T. Huff, Acoustic attenuation of hybrid silencers, J. Sound Vib. 262 (2003) 509–527, doi:10.1016/S0022-460X(03)00109-3.

[2] W.P. Williams, R. Kirby, J. Hill, M. Åbom, C. Malecki, Reducing low frequency tonal noise in large ducts using a hybrid reactive-dissipative silencer, Appl. Acoust. 131 (2017) 61-69, doi 10.1016/j.apacoust.2017.10.018.

[3] M.A. Galland, B. Mazeaud, N. Sellen, Hybrid passive/active absorbers for flow ducts, Appl. Acoust. 66 (2005) 691-708, doi 10.1016/j.apacoust.2004.09.007.

[4] G.C. Ma, P. Sheng, Acoustic metamaterials: From local resonances to broad horizons, Sci. Adv. 2 (2016) 1501595, doi10.1126/sciadv.1501595.

[5] Y.F. Tang, S.W. Ren, H. Meng, F.X. Xin, L. Huang, T.N. Chen, C.Z. Zhang, T.J. Lu, Hybrid acoustic metamaterial as super absorber for broadband low-frequency sound, Sci. Rep. 7(2017) 43340, doi 10.1038/srep43340.

[6] S.B. Huang, E.M. Zhou, Z.L. Huang, P.F. Lei, Z.L. Zhou, Y. Li, Broadband sound attenuation by metaliner under grazing flow, Appl. Phy. Lett. 118 (2021) 063504, doi 10.1063/5.0042228.

[7] L. Cremer, Theory regarding the attenuation of sound transmitted by air in a rectangular duct with an absorbing wall, and the maximum attenuation constant produced during this process, Acustica 3 (1953) 249–263.

[8] B.J. Tester, The optimisation of modal sound attenuation in ducts, in the absence of mean flow, J. Sound Vib. 27 (1973) 477–513, doi 10.1016/S0022-460X(73)80358-X.

[9] A.M.N. Spillere, Z. Zhang, J.A. Cordioli, M. Åbom, H. Bodén, Optimum impedance in the presence of an inviscid sheared flow, AIAA J. 57 (2019) 1044-1054, doi 10.2514/1.J057526.

[10] Z. Zhang, H. Bodén, M. Åbom, The Cremer impedance: An investigation of the low frequency behavior, J. Sound Vib. 459 (2019) 114844, doi 10.1016/j.jsv.2019.07.010.

[11] E. Perrey-Debain, B. Nennig, J.B. Lawrie, Mode coalescence and the Green's function in a two-dimensional waveguide with arbitrary admittance boundary conditions, J. Sound Vib. 516 (2022) 116510, doi 10.1016/j.jsv.2021.116510.

[12] K. Billon, E. De Bono, M. Perez, E. Salze, G. Matten, M. Gillet, M. Ouisse, M. Volery, H. Lissek, J. Mardjono, M. Collet, In-flow acoustic characterization of a 2D active liner with local and non-local strategies, Appl. Acoust. 191(2022) 108655, doi 10.1016 /j.apacoust.2022.108655.

[13] J.S. Li, L. Fok, X.B. Yin, G. Bartal, X. Zhang, Experimental demonstration of an acoustic magnifying hyperlens, Nat. Mater. 8(12) (2009) 931-934, doi 10.1038/NMAT2561.

[14] S.A. Cummer, J. Christensen, A. Alù, Controlling sound with acoustic metamaterials, Nat. Rev. Mater. 1(3) (2016) Art. No. 16001, doi: 10.1038/natrevmats.2016.1.

[15] H. Nassar, B. Yousefzadeh, R. Fleury, M. Ruzzene, A. Alù, C. Daraio, A.N. Norris, G. Huang, M.R. Haberman, Nonreciprocity in acoustic and elastic materials, Nat. Rev. Mater. 5 (2020) 667–685, doi 10.1038/s41578-020-0206-0.
[16] M.R. Haberman, A.N. Norris, Acoustic Metamaterials, Acoust. Today 12 (3) (2016), Acoustical Society of America, doi 10.1063/PT.3.3198.
[17] C.Q. Wang, L. Huang, On the acoustic properties of parallel arrangement of multiple micro-perforated panel absorbers with different cavity depths, J. Acoust. Soc. Am. 130 (2011) 208-218, doi 10.1121/1.3596459.
[18] X. Wang, C.M. Mak, Wave propagation in a duct with a periodic Helmholtz resonators array, J. Acoust. Soc. Am. 131 (2012) 1172–1182, doi: 10.1121/1.3672692.
[19] H.M. Yu, S.K. Tang, Sound transmission across a narrow sidebranch array duct muffler at low Mach number, J. Acoust. Soc. Am. 148 (2020) 1692-1702, doi 10.1121/10.0001993.
[20] J. Boulvert, T. Humbert, V. Romero-Garcia, G. Gabard, E.R. Fotsing, A. Ross, J. Mardjono, J.P. Groby, Perfect, broadband, and sub-wavelength absorption with asymmetric absorbers: Realization for duct acoustics with 3D printed porous resonators, J. Sound Vib. 523 (2022) 116687, doi 10.1016/j.jsv.2021.116687.
[21] T. Bravo, C. Maury, Causally-guided acoustic optimization of single-layer rigidly-backed micro-perforated partitions: Theory, J. Sound Vib. 520 (2021a) 116634, doi 10.1016 /j.jsv.2021.116634.
[22] T. Bravo, C. Maury, Causally-guided acoustic optimization of rigidly-backed micro-perforated partitions: Case studies and experiments, J. Sound Vib. 523 (2021b) 116735, doi 10.1016 /j.jsv.2021.116735.
[23] C. Caloz, Z.L. Deck-Leger, Spacetime Metamaterials-Part I: General Concepts, IEEE Trans. Anten. Propag. 68 (2020) 1569-1582, doi 10.1109/TAP.2019.2944225.
[24] C. Caloz, Z.L. Deck-Leger, Spacetime Metamaterials-Part II: Theory and Applications, IEEE Trans. Anten. Propag. 68 (2019) 583-1598, doi 10.1109/TAP.2019.2944216.
[25] A. Shapere, F. Wilczek, Classical time crystals, Phys. Rev. Lett. 109(15) (2012) 1–4, doi: 10.1103/PhysRevLett.109.160402, doi 10.1103/PhysRevLett.109.160402.
[26] X. Guo, H. Lissek, R. Fleury, Improving sound absorption through nonlinear active electroacoustic resonators, Phys. Rev. Appl. 13 (2020) 01418, doi 10.1103 /PhysRevApplied.13.014018.
[27] Y. Zhang, C.Q. Wang, L. Huang, Tuning of the acoustic impedance of a shunted electro-mechanical diaphragm for a broadband sound absorber, Mech. Sys. Sig. Proc. 126 (2019) 536-552, doi 10.1016/j.ymssp.2019.02.049.
[28] Y. Zhang, K. Wu, C. Wang, L. Huang, Towards altering sound frequency at will by a linear meta-layer with time-varying and quantized properties, Commun. Phys. 4 (2021) 220, doi 10.1038/ s42005-021-00721-1.
[29] L. Huang, A theory of reactive control of low-frequency duct noise, J. Sound Vib. 238(2000) 575-594, doi 10.1006/jsvi.2000.3090.
[30] Y. Zhang, C.Q. Wang, L. Huang, A tunable electromagnetic acoustic switch, Appl. Phys. Lett. 116 (2020) 183502, doi 10.1063/5.0008532.
[31] K. Wu, L. Huang, X. Zhang, X. Liu, C. Wang, Y. Zhang, Broadband and extremely low frequency sound isolation by a programmable shunted electromechanical diaphragm with force dipole eff ect, Int. J. Mech. Sci. 200 (2021) 106447, doi 10.1016/j.ijmecsci.2021.106447.
[32] C.Q. Wang, L. Huang, Time-domain simulation of acoustic wave propagation and interaction with flexible structures using Chebyshev collocation method, J. Sound Vib. 331 (2012) 4343–4358, doi 10.1016/j.jsv.2012.05.015.
[33] Y. Miki, Acoustical properties of porous materials - modifications of Delany-Bazley models, J. Acoust. Soc. Jpn (E), vol. 11(1) (1990) 19-24, doi 10.1250/ast.11.19.
[34] Y.H. Chiu, L. Cheng, L. Huang, Drum-like silencers using magnetic forces in a pressurized cavity, J. Sound Vib. 297 (2006) 895-915, doi 10.1016/j.jsv.2006.05.006.